Journal Pre-proof

Multi-banded pumice in the Campo de la Piedra Pómez rhyolitic ignimbrite (Southern Puna plateau): Pre-eruptive physical and chemical interactions between mafic and rhyolitic melts

L. Bardelli, M. Arnosio, W. Báez, N. Suzaño, R. Becchio, J. Viramonte, E. Bustos, E. Bertea

1 **Multi-banded pumice in the Campo de la Piedra Pómez rhyolitic ignimbrite**

2 **(Southern Puna Plateau): Pre-eruptive physical and chemical interactions between**

3 **mafic and rhyolitic melts**

4 **L. Bardelli*[1-2], M. Arnosio[1-2], W. Báez[1-2], N. Suzaño[3], R. Becchio[1-2], J. Viramonte[1-2], E. Bustos[1-2],**

5 **E. Bertea[1-2]**

6 [1] Geonorte Institute, National University of Salta

7 [2] IBIGEO-CONICET, Salta

8 [3] National University of Jujuy

9 [*] Corresponding author: Tel +54 3876360436 e-mail: lorenzobardelli4@gmail.com; address: Avenida Bolivia 5150, CP

10 4400, Salta, Argentina.

11 **Abstract**

12 The rhyolitic Campo de la Piedra Pómez ignimbrite crops out in the Southern Puna of NW Argentina

13 and it is related to the youngest caldera-complex (Cerro Blanco caldera complex) of the Central Andes

14 (73 - 4 kyr). The presence of rhyolitic pumice and mafic enclaves with different compositional and

15 textural features, which variability can be observed within a single juvenile clast (multiple-banded

16 pumice), characterized these deposits. The enclaves are associated with hybrid (trachydacitic) pumice

17 and sporadic remnants of rhyolitic material included in the trachydacite. To unravel the possible role of

18 the mafic recharge as eruption trigger, the occurrence of mixing events and the mechanisms of enclave

19 formation, we studied the enclaves and silicic pumice material (petrography, whole rock analyses,

20 mineral and glass chemistry) to decipher the magmatic interaction between the host rhyolitic melt and

21 the enclave-forming magmas. Results allowed recognizing two main mafic recharge events. During the

22 first episode, the mixing of the rhyolite with the injecting magma generated sporadic dacitic products.

23 Mixing was favored by the relatively high temperature of both the injecting magma and the rhyolitic

24 melt, as revealed by clinopyroxene-liquid, plagioclase-liquid and two-pyroxene geothermometers ($\geq$

25 875 °C). The second mafic recharge event involved magma that remained confined at the bottom of the

26   reservoir and crystallized with differential cooling rates. At the interface with the silicic host, the

27   magma generated sub-millimetric mineral assemblage in which amphibole has normally zoned rims.

28   Differently, within the body of the mafic intrusion, crystallization proceeded with a lower undercooling

29   degree, generating a coarser crystalline assemblage in which amphibole crystals do not display zoning.

30   The convergence of different thermobarometric models (applied to the rhyolite, trachydacite, and

31   enclaves) suggests that these magmas interacted at a crustal depth of ca. 2.7 Kbar, here interpreted as

32   the base of the Campo de la Piedra Pómez rhyolitic reservoir (~ 10 Km b.s.l.). A time lapse occurred

33   between the last mafic recharge and the eruptive events, where the felsic magma cooled down to ~ 800

34   °C and the amphibole re-equilibration took place.

35   **Key words:** mafic recharge, magma mixing, quenching textures, amphibole zoning, thermobarometry

36   **1 Introduction**

37   Mafic enclaves are typical products of arc-related volcanic rocks of intermediate to rhyolitic

38   compositions (Heiken and Eichelberger, 1980; Bacon, 1986; Murphy et al., 1998; Mortazavi and

39   Sparks, 2004). Their study helps to disclose different aspects of volcanic systems, from the role of

40   mafic recharge as eruption trigger (Pallister et al., 1992; Murphy et al., 1998, 2000; Streck and

41   Grunder, 1999; Scruggs and Putirka, 2018) to the mechanisms of magma interaction (Bacon, 1986;

42   Clynne, 1999; Coombs et al., 2003; Browne et al., 2005; Martin et al., 2006; Morgavi et al., 2013,

43   2016; Plail et al., 2014, 2018; Hernando et al., 2016). Specifically, the textural characteristics of the

44   enclaves (shape, groundmass texture, crystallinity, vesiculation), provide information about the thermal

45   history of the enclave-forming magma/s, which can be recorded in the morphology of groundmass

46   crystals (from acicular to less elongated habits) and modal content (Bacon, 1986; Coombs et al., 2003;

47   Mortazavi and Sparks, 2004; Browne et al., 2005; Martin et al., 2006; Bacon, 2011; Shea and Hammer,

48   2013; Plail et al., 2014, 2018). Additionally, the enclave compositional features (major element

49   contents, mineral and glass composition), together with those of the hosting magma, could help to

50 disclose the occurrence of magma mingling and mixing episodes (crystal transfer, chemical

51 hybridization) during pre- and syn-eruptive phases (Eichelberger, 1980; Bacon, 1986; Couch et al.,

52 2001; Martin et al., 2006; Arnosio, 2010; Hernando et al., 2016).

53 The occurrence of mafic recharge has been suggested for the rhyolitic Campo de la Piedra Pómez

54 Ignimbrite (CPPI) eruption (Báez et al., 2015, 2020a), which is part of the youngest (~73 – 4 myr)

55 calderic system of Argentinian Central Andes, the Cerro Blanco Volcanic Complex (CBVC, Arnosio et

56 al., 2005; Montero-López et al., 2010, Báez et al., 2015, 2020a). The presence within the ignimbrite of

57 mafic enclaves, which form multi-banded pumice fragments of different colors, textures, and

58 compositions (alternation of basaltic trachyandesite, trachydacite and rhyolite), provides an interesting

59 opportunity to investigate the consequences of mafic injections into this rhyolitic system of the

60 Argentinian Puna plateau, both in terms of magma mixing occurrence and possible recharge-induced

61 eruption trigger. Thus, we investigated the textural and petrological features (crystal contents and

62 textures, whole-rock analyses, mineral and glass compositions) of both mafic enclaves and rhyolitic

63 pumices from the CPPI. We then applied a suite of thermobarometric models based on (i) amphibole

64 composition (Ridolfi and Renzulli, 2012); (ii) mineral-liquid equilibrium such as olivine-liquid (Putirka

65 et al., 2007; Putirka, 2008), clinopyroxene-liquid (Putirka, 2008), orthopyroxene-liquid (Putirka, 2008)

66 and plagioclase-liquid (Putirka, 2003, 2005, 2008) models; (iii) mineral-mineral equilibrium such as

67 clinopyroxene-orthopyroxene (Putirka, 2008) and plagioclase-alkali feldspar (Putirka, 2008) models;

68 and (iv) zircon-saturation (Watson and Harrison, 1983) model. The purpose of this work is (i) to

69 provide an interpretation for the observed mineral disequilibrium assemblages and textures, (ii) to

70 unreavel the occurrence of hybridization (chemical mixing) between the enclave-forming magma/s and

71 the rhyolitic host, (iii) to reconstruct the thermal history of the different magmas, defining the

72 mechanisms of genesis of the enclave types, iv) to constrain the physical conditions of the magmas that

73 interacted in the Campo de la Piedra Pómez magmatic system. Finally, the possible temporal

74 coincidence between the last injection of mafic magma and the beginning of the Plinian eruption is

75 discussed.

76 **2 Geological background**

77 Central Andes is one of the most important volcanic zones on Earth, where Cenozoic volcanism is

78 generated by the subduction of the Nazca plate beneath South America (James, 1971; de Silva, 1989).

79 The most prominent feature of the Central Volcanic Zone (CVZ;18-27 °S; Stern, 2004) is the

80 Altiplano-Puna plateau, an extensive zone of 3800 meters a. s. l. which has been interested during Late

81 Miocene - Holocene by huge magmatism and intense volcanic activity (Kay and Coira, 2006; de Silva

82 and Gosnold, 2007; Schnurr et al., 2007; Kay et al., 2010; Guzmán et al., 2014; Lucci et al., 2018). The

83 estimated crustal thickness for this area of the plateau is between 50-80 Km (Bianchi et al., 2013; Heit

84 et al., 2014). The CPPI crops out in the back-arc area of the Southern Puna plateau, close to the

85 boundary between the Central Volcanic Zone and the volcanism-free flat-slab region towards the south

86 at ~27 °S (Barazangi and Isacks, 1976, Jordan et al., 1983; Fig. 1). It is part of the Cerro Blanco

87 Volcanic Complex (CBVC), which represent the youngest volcanic activity related to the Upper

88 Miocene-Quaternary La Hoyada Volcanic Complex (Seggiaro et al., 2000; Montero-López et al., 2010;

89 Báez et al., 2015; 2020b Bustos et al., 2019; Fig. 1). Volcanic activity developed in this area since Late

90 Miocene (~9 Ma) with the emission of predominantly andesitic and dacitic products (Kay et al, 2006;

91 Montero-López et al., 2010; Guzmán et al., 2014; Bustos et al., 2019) and associated minor rhyolites

92 (Siebel et al., 2001; Schnurr et al., 2007). During Pleistocene-Holocene an important bimodal

93 volcanism began, with the generation of numerous mafic centers (e.g. Viramonte et al., 1984; Kay et

94 al., 1994; Risse et al., 2008; Maro et al., 2017a, b, c; Báez et al., 2017b; Filipovich et al., 2019; Hagg et

95 al., 2019), and rhyolitic volcanic episodes represented by the CBVC (comprising the CPPI) and by the

96 eruptive centers of Chascón and Cueros de Purulla (Seggiaro et al., 2000, Montero-Lopez et al., 2010,

97 Báez et al., 2015; 2017a; 2020b; Fig. 1). The CBVC is a nested-caldera system formed by two plinian

98   events, the oldest CPPI (~73 kyr) and the Holocene Cerro Blanco Ignimbrites (~ 4 kyr) and lava domes.

99   The monogenetic mafic volcanoes in the study area surround the CPPI to the west, east and north, but

100 are not present within the immediate proximity of the ignimbrite outcrops (Risse et al., 2008; Maro et

101 al., 2017a,b,c; Filipovich et al., 2019; Haag et al., 2019; Fig. 1).

102 Pre-Ordovician and Ordovician metamorphic rocks compose the basement of the area, together with

103 volcanic and volcanoclastic units (Seggiaro, 2000; Lucassen and Becchio, 2003; Suzaño et al., 2014).

104 Pre-Ordovician rocks crop out to the southeast of the study area, while Ordovician basement is present

105 to the west and is composed by metamorphic, sedimentary and volcanic units intruded by basic and

106 ultrabasic rocks (Seggiaro, 2000; Lucassen and Becchio, 2003; Suzaño et al., 2014). At upper

107 stratigraphical levels, basement is composed of turbiditic sequences (Aceñolaza et al., 1976), and of

108 Permian and Eocene continental sedimentary rocks (Fernándes Seveso et al., 1991; Turner, 1961).

109 Báez and coworkers (2015, 2020a) described in detail the architecture of the CPPI and its facies, and

110 defined two eruptive events (CPPI Phase I and Phase II; Fig. 2a), with a total estimated volume of ca.

111 35 Km^3 (DRE). Both phases are composed predominantly by rhyolitic pumice and differ in the

112 composition and abundance of the lithic component. Phase II is characterized by a slightly less evolved

113 rhyolitic pumice population and by greater abundance of mafic material (banded pumice and sparse

114 enclaves) than Phase I deposits, in which mafic material is sporadic (see Section 4.1 for major details).
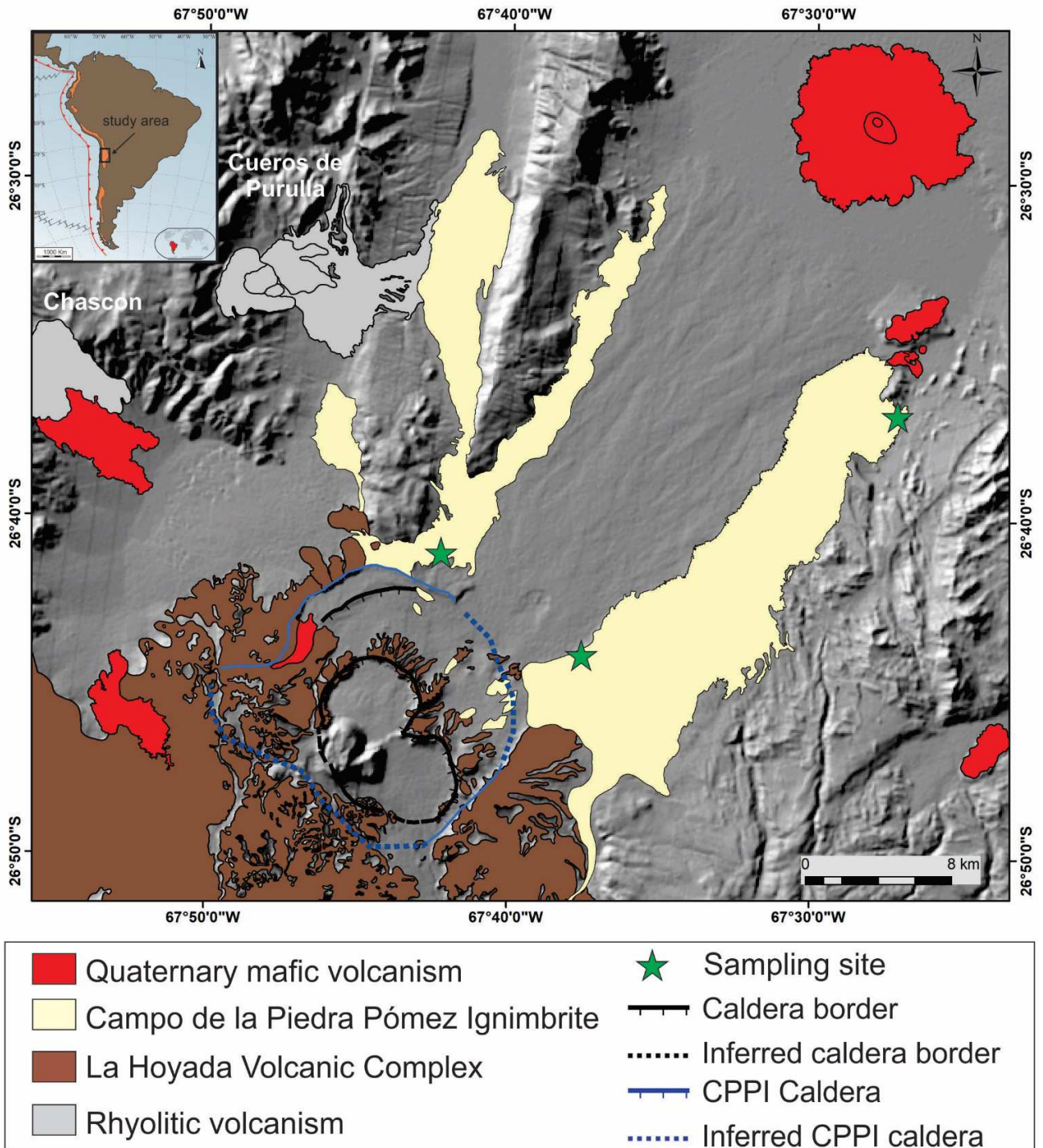
Figure 1. Schematic map of the CPPI outcrops and its surroundings. Upper-left inset indicates the position of the study area within the Central Volcanic Zone of the Andean chain (black arrow). The inferred CPPI caldera border is from Báez et al. (2020a).

3 Analytical methods

120 During the fieldwork carried out in December 2017, an extensive sampling of the distinct juvenile

121 clasts from proximal and distal ignimbrite facies of both eruptive Phases I and II (Figs. 1) was

122 developed. Whole-rock analyses (n= 20) were performed on selected preserved samples unaffected by

123 weathering or alteration. They were reduced in a jaw crusher, fine-powdered in a Herzog mill with

124 tungsten carbide bowl and dried at 105 °C for 24 h in an electric oven. Major elements content

125 determinations (Si, Ti, Al, Fe, Mn, Mg, Ca, Na, K, P) were carried out at the ALS Minerals Laboratory

126 by inductively coupled plasma mass spectrometry (ICP-MS) following a Lithium

127 metaborate/tetraborate fusion and nitric acid digestion. Additional information about detection limits

128 and methodology are available on www.alsglobal.com. Whole rock analyses were normalized to a 100

129 % volatile-free basis, and Fe contents are expressed as total FeO. Petrographic study and mineral point

130 counting (about 800 point each thin section) were made on 20 thin polished section at the National

131 University of Salta (UNSa, Argentina), which were then selected (n = 8) for microprobe analyses.

132 These were performed with a Jeol JXA-8230 electron microprobe at the LAMARX (Laboratorio de

133 Microscopía Electrónica y Análisis por Rayos X) at the National University of Córdoba (UNC,

134 Argentina). Measurements include Si, Ti, Al, Fe, Mn, Mg, Ca, Na, K, P, F, Cl. Current and voltage

135 used were 10 nA and 20 kV respectively, with counting times of 20 s for silicates, using natural and

136 synthetic materials as standard and a beam size of 10 - 5 microns for minerals and glass, respectively. F

137 and Na were analyzed first to reduce the loss during measurement. Glass analyses were normalized to

138 100 % before the interpretation of the data.

139 **4 Results**

140 *4.1. CPPI pumice and enclave description*

141 The presence within the CPPI of different juvenile clasts (pumice and enclaves) and their main

142 petrographic features were described by Báez et al. (2015). A white to light grey, poorly crystalline

143 vesiculated pumice (WP = white pumice) displays rhyolitic composition and represents the main

144 constituent of both CPPI phase I and II (~ 90 %, Fig. 2a, b). Deposits of Phase I contain small amounts

145 of a dark-grey to black microcrystalline sub-rounded enclave (BE = black enclave) which occur with

146 low abundance (< 1 %) as crenulated inclusions within WP and as isolated clasts in the ignimbrite (Fig.

147 2c). In addition to WP, deposits of eruptive Phase II contain a vesiculated beige pumice (BP = beige

148 pumice) which is associated with texturally different mafic enclaves that alternate forming multiple-

149 banded pumice clasts (up to 60 cm; Fig. 2d, e). Among these bands (i.e, the enclaves), we recognized

150 and described three different mafic types characterized by peculiar colors and textures. The first type is

151 a dark-grey to black enclave equivalent to BE of CPPI phase I (we also refer to these products as BE).

152 It forms partially dismembered layers and pillow-like millimetric blobs in the banded pumice clasts

153 and, to a lesser extent, within WP (Fig. 2f-h). The second and third types constitute centimetric to

154 decimetric brown layers in banded pumice and frequently are in contact with each other (Fig. 2d-g). On

155 the basis of crystal size, we refer to these two enclave types as a coarse brown enclave (CBE) and a

156 fine brown enclave (FBE). CBE is more abundant than FBE (~ 5 Vol % and ~ 1 Vol %, respectively)

157 and contains, sparsely, dark crystal-rich inclusions composed of millimetric biotite + amphibole

158 crystals and vesiculated glass (Fig. 2 h). Some multi-banded pumiceous clasts exhibit the presence of

159 all enclave and pumice types (Fig. 2e, g), which frequently are intensely intermingled (Fig. 2 h).

160 Commonly, beige pumice (BP) contains amygdale-like inclusions of WP blobs (Fig. 2 g).

161
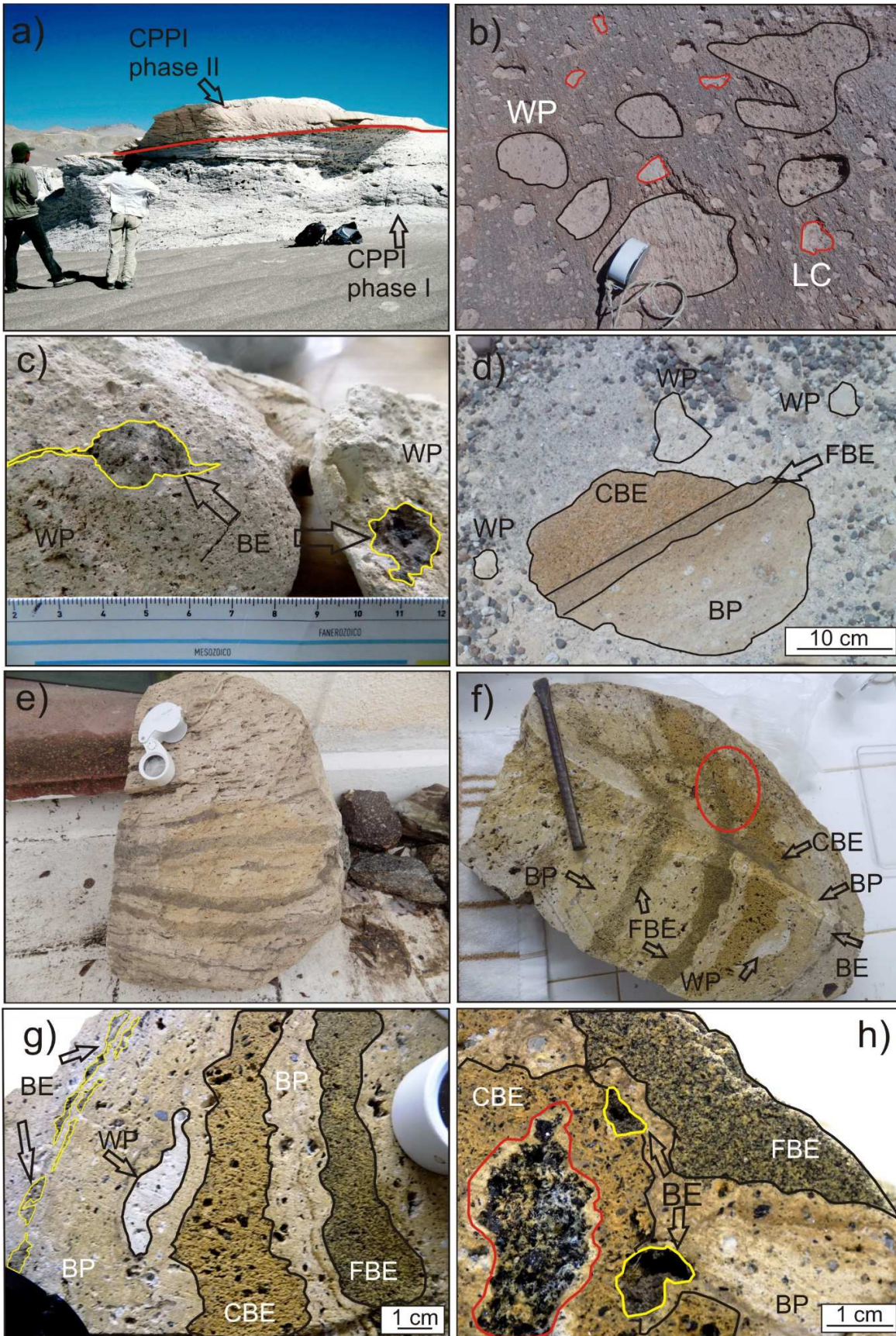
162　Figure 2. a) Outcrop of the CPPI facies in which the division between the two volcanic phases (I and II) is indicated (red
163　line). b) Detail of a CPPI phase I outcrop, in which sparse WP clasts (black outline) and lithic fragments from the Miocene
164　Rosada Ignimbrite (Báez et al., 2015; LC; red outline) can be observed. c) WP clasts containing crenulated BE pillow-like
165　blobs (from CPPI Phase I). d) Detail of the proximal CPPI facies of Phase II with banded pumice (CBE + FBE + BP; see
166　text for explanations) and sparse WP clasts. e) Decimetric multiple-banded pumice clast collected in proximal CPPI facies
167　of phase II. f) Multiple-banded pumice clast in which all the juvenile types can be observed. g) Detail of figure 2f in which
168　partially dismembered layers of BE (yellow outline), an amygdale-like WP inclusion and the alternation of FBE, CBE and
169　BP (black outline) can be observed. h) Detail of a crystal-rich inclusion within CBE (red outline); intense intermingling
170　among FBE, CBE, BP and BE can be observed.

171　*4.2. Petrography*

172　We summarize in this section the principal petrographic features of the CPPI pumice and enclave types.

173　Mineral name abbreviations are according to Whitney and Evans (2010), and mineral modal

174　calculations were calculated excluding the glass and vesicles percentages (Table 1).

175　Table 1

176　*4.2.1. White pumice (WP)*

177　WP is a porphyritic poorly crystalline rhyolite, with a simple phenocrysts assemblage composed of Pl

178　(30-60 %) + Kfs (20-55 %) + Bt (5-20 %) + Qz (~0-10%) + Opq (~5 %) + Cpx (~ 1 %) + accessory Ap

179　+ Zrn, immersed in a vesiculated holohyaline glass. Some pumice display a low porphyritic index (P.I.

180　<5 %) and high crystal fragmentation degree, with micrometric-sized phenocryst fragments of feldspars

181　and quartz plus minor biotite (~0.2-0.4 mm; Fig. 3a). Most WP specimens exhibit larger and unbroken

182　phenocryst populations (1-2 mm) and higher crystal contents (P.I = 15-20%; Fig. 3b). Feldspars are

183　euhedral and occur as isolated grains and as minor glomerophyric aggregates. Some plagioclase

184　phenocrysts exhibit optical low-banded oscillatory zoning, occasionally a slight patchy character, and

185　lack evident resorption surfaces (e.g. Streck, 2008) when observed at back-scattered electron images

186　(BSE; Fig. 3c, d), while other grains are homogeneous. Quartz is present as partially resorbed

187　subehdral grains with millimetric dimensions (up to 1.5 mm; Fig. 3b). Reddish biotite grains are

188　laminar ($\leq$ 1 mm length) and euhedral (Fig. 3b, d, f), as well as clinopyroxene crystals (1-2 mm), which

189　is hosting biotite, oxides and apatite inclusions (Fig. 3e, f). Oxides (magnetite and ilmenite) are present

190   as rounded subehdral grains ($\leq$ 0.5 mm), and display, when observed with BSE images, slight

191   development of exsolution lamellae or homogeneous texture (Fig. 3e, f). Accessory apatite (<0.5%)

192   normally occurs as inclusions in plagioclase and clinopyroxene (~ 150 micron; Fig. 3e). Rare

193   orthopyroxene and olivine grains occur within WP (<< 1 %), displaying narrow reaction rims formed

194   by amphibole microcrystals or by an undefined opaque rim.

195
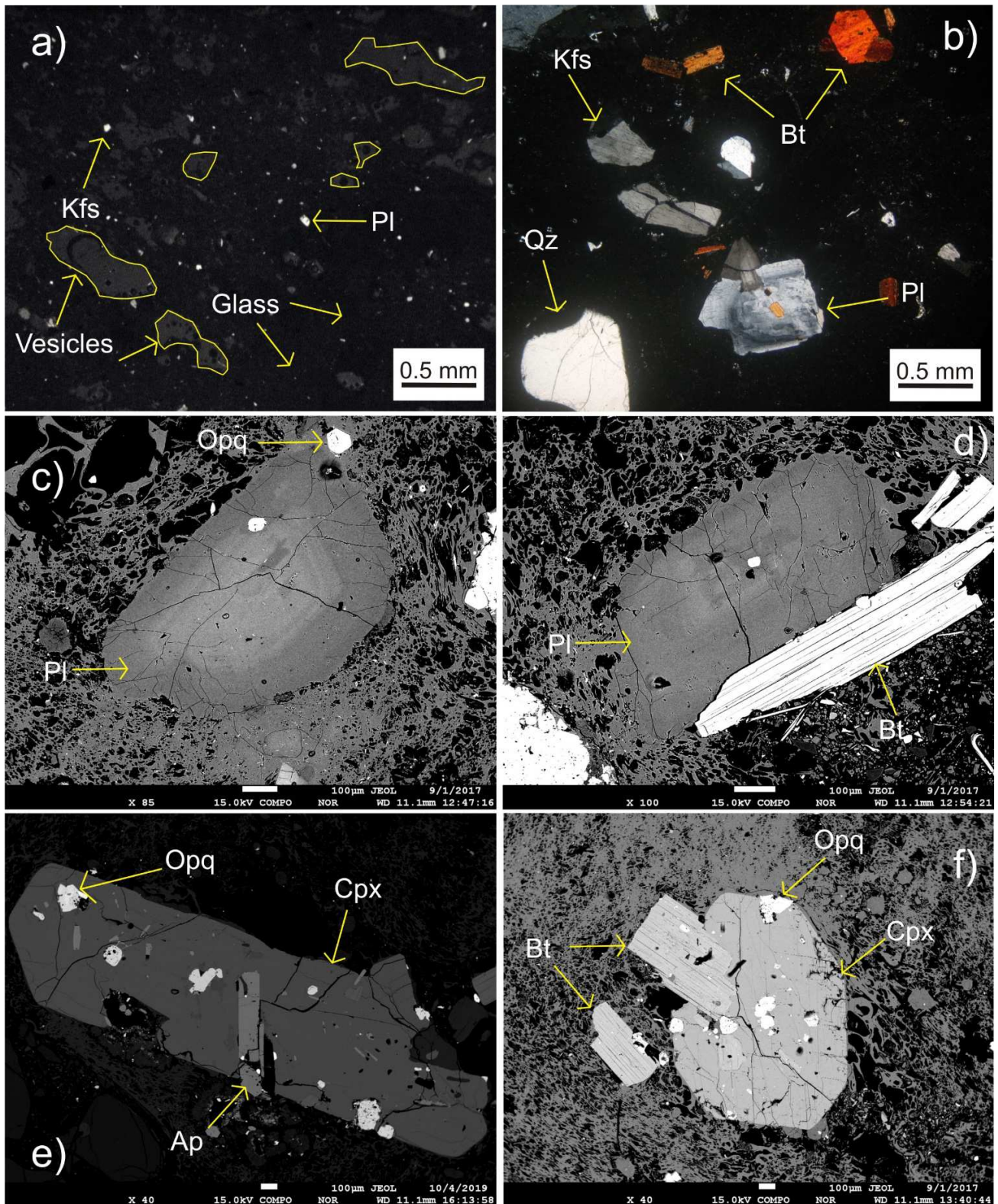
Figure 3. Petrographic features of rhyolitic WP. a) Microphotograph (cross-polarized lights) of a WP sample with low P.I: and high crystal fragmentation degree; yellow outline indicates vesiculation. b) Microphotograph (cross-polarized lights) of a WP sample with higher Porphyritic Index. c) BSE image of plagioclase phenocryst with oscillatory texture. d) BSE image of oscillatory-textured plagioclase with associated biotite phenocrysts. e) BSE image of euhedral clinopyroxene phenocrysts

201 showing opaque minerals and apatite inclusions. f) BSE image of euhedral clinopyroxene phenocrysts with opaque
202 (magnetite + ilmenite) minerals and biotite inclusions.

203

204 *4.2.2. Beige pumice (BP)*

205 Beige pumice shows porphyritic texture and a holohyaline vesiculated glass, displaying a complex

206 mineralogical assemblage composed of Pl (30-45 %) + Bt (~ 20 %) + Kfs (~ 10) + Amp (5-10 %) +

207 Opx (5 %) + Opq (< 5 %) + Cpx (~ 1 %) + Ol (traces). Similarly to WP, BP displays variable P.I.

208 (from ~10 to 20 %; Fig. 4a-d). Plagioclase crystals (0.5-1.5 mm) normally present optical oscillatory

209 zoning or are homogeneous (Fig. 4b, h). Tabular reddish biotite grains (up to 2 mm) resemble

210 texturally those from WP samples (Fig. 4a), as well as K-feldspar crystals (Fig. 4a, b). Clinopyroxene

211 (normally sub-millimetric) occur with subehdral habits with narrow amphibole reaction rims (as well

212 as olivine; Fig. 4e, f), and can form small glomerocrystic aggregates. Pyroxene grains (both Cpx and

213 Opx) were also observed within partially dismembered microlite-rich (Amp + Pl) glassy blobs

214 contained within BP (Fig. 4c, d). Amphibole is euhedral, millimetric in size (1-1.5 mm) and unzoned,

215 and is frequently associated with orthopyroxene (normally present as inclusion within amphibole; Fig.

216 4g) and with plagioclase (Fig. 4h).
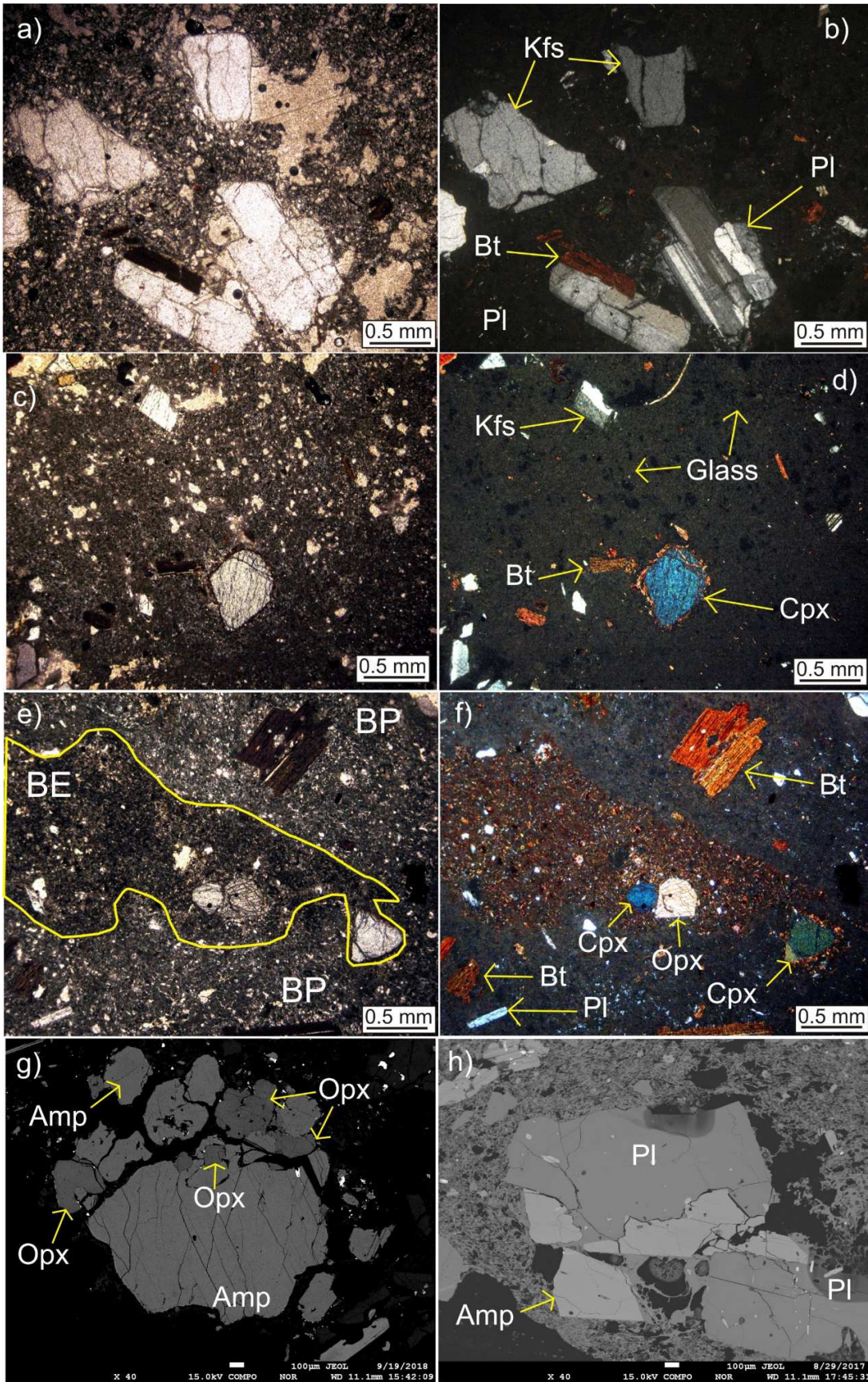
218 Figure 4. BP petrographic features. a) Microphotograph (parallel-polarized light) showing the association plagioclase + K-
219 feldspar + biotite, all immersed in a holoyaline groundmass. b) Same view of (a) taken with cross-polarized light. c)
220 Microphotograph (parallel-polarized light) of a low P.I. sample with a clinopyroxene grain rimmed by a narrow amphibole
221 reaction rim. d) Same microphotograph of (c) taken with cross-polarized light. e) Microphotograph (parallel-polarized light)
222 of an irregular blob of quenched glass (microlite-rich groundmass + pyroxene crystals). f) Microphotograph of the same
223 view of (e) taken with cross-polarized light. g) BSE image of amphibole + orthopyroxene association. h) BSE image of
224 amphibole + plagioclase association.

225 *4.2.3. Black enclave (BE)*

226 BE is a porphyritic rock (P.I. 15-20%, Fig. 5a) and exhibits a complex mineral assemblage consisting

227 of Pl (30-40 %) + Cpx (~25-30 %) + Opx (10-15 %) + Ol (5 – 10 %) + Opq (< 5 %) + Amp (1 - 5 %) +

228 accessory Kfs, Qz and Bt. The matrix is a micro-vesiculated hialopylitic glass formed by plagioclase

229 laths and tabular to acicular amphibole microlites which, occasionally, can occur in contact with each

230 other (50-150 micron; Fig. 5b, c). The proportion between microlites and glass is about 50-60%

231 crystals and 40-50% glass (vesicle-free), and variation in the dimensions of the matrix minerals

232 towards the enclave edges was not observed. Clinopyroxene and orthopyroxene occur as isolated grains

233 or in crystal aggregates (up to n = 100 crystals; Fig. 5d) and exhibit similar textural features like sub-

234 millimetric to millimetric dimensions (~0.5-1 mm), euhedral to subehdral habits and diffuse amphibole

235 reaction rims (Fig. 5e). Rare orthopyroxene grains reach larger dimensions (up to 3 mm) and show

236 partially resorbed rims surrounded by amphibole microcrystals and orthopyroxene grains that are

237 texturally similar to the phenocrysts (Fig. 5-A1 of Supplementary Material). Olivine consists of

238 rounded crystals (~0.8-1.2 mm) always surrounded by a narrow amphibole reaction rim (Fig. 5f) or by

239 an undefined thin opaque rim. Plagioclase exhibits variable textural and compositional features.

240 Microlites in the matrix form about the 50% of the whole plagioclase population (Fig. 5b, c).

241 Millimetric subehdral to euhedral crystals (up to 1.3 mm; Fig. 5g), partially resorbed sub-millimetric

242 grains (sieve-textured) with fresh overgrowth (~20-30 micron; Fig. 5i) and anhedral crystals compose

243 the remnant 50 % of plagioclase population (Fig. 5h). Amphibole occurs as microlites in the matrix and

244 as reaction rims (100-200 micron) around pyroxene, olivine and opaque crystals (Fig. 5b, c, e, f, l).

245 Large amphibole phenocrysts (up to 3 mm) with inclusions of plagioclase and olivine (Fig. 5k) and rare

246 biotite and K-feldspar grains (< 1 mm) were sporadically observed (Fig. 5j, k, Fig. 5-A2 of

247 Supplementary Material). Occasionally, sparse blobs of holohyaline glass containing subehdral K-

248 feldspar grains are separated from the typical BE groundmass by a reaction rim of pyroxene

249 microcrystals (Fig. 5j). Opaque minerals exhibit sub-millimetric dimensions (0.5-0.8 mm), subehdral to

250 anhedral habits, and display well-developed exsolution textures when observed at BSE imaging (Fig.

251 5l).
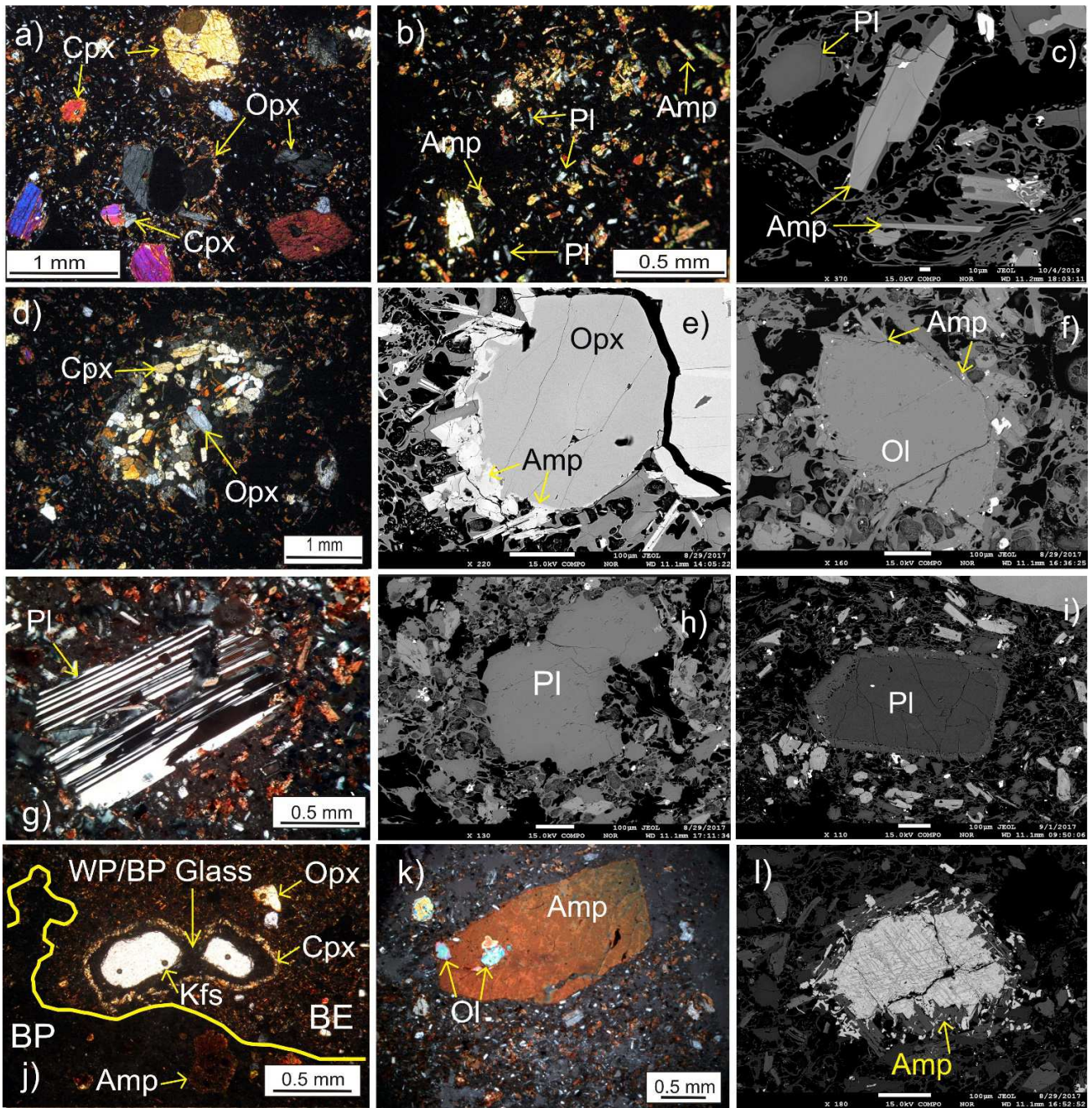
Figure 5. Petrographic features of BE. a) Microphotograph (cross-polarized light) showing subehdral clinopyroxene + orthopyroxene phenocrysts rimmed by amphibole microlites and immersed in a hialopylitic glass. b) Detail microphotograph (cross-polarized light) of the quenched groundmass (Amp + Pl). c) BSE image of groundmass showing two different amphibole habits (from tabular to acicular) and plagioclase laths, all sparse in a vesiculated glass. d) Microphotograph (cross-polarized light) of a clinopyroxene + orthopyroxene glomerocryst aggregate. e) BSE image of an orthopyroxene grain rimmed by amphibole microlites. f) BSE image of a sub-rounded olivine phenocryst rimmed by amphibole microlites. g) Microphotograph (cross-polarized light) of a slightly resorbed plagioclase crystal. h) BSE image of an anhedral plagioclase grain. i) BSE image of a partially resorbed (sieve-textured) plagioclase grain with fresh overgrowth. j) Microphotograph (cross-polarized light) of K-feldspar + holoyaline glass with pyroxene reaction rim. k) Microphotograph (cross-polarized lights) of a large amphibole phenocryst. l) BSE image of a magnetite crystal with diffuse exsolution texture and amphibole reaction rims.

264 *4.2.4. Fine brown enclave (FBE)*

265 FBE exhibits an equigranular texture and a micro-vesiculated glass (Fig. 6a, b). Crystal population

266 comprises Pl (40-50 %) + Amp (~40 %) + Bt (~10-15 %) + Opq (~5 %) + Ap (traces), with a P.I. of

267 ~35 % and general sub-millimetric crystal dimensions (0.2-0.8 mm, rarely up to 1 mm; Fig. 6a).

268 Amphibole occurs as subehdral to euhedral prismatic and tabular crystals which display diffuse

269 concentric zoning pattern (BSE images) formed by darker cores and brighter rims (Fig. 6c, d).

270 Amphibole occur mainly as isolated grains in the glass and occasionally associated with plagioclase

271 and biotite (Fig. 6e). Plagioclase displays tabular subehdral to euhedral shapes, showing slight optical

272 oscillatory zoning or homogeneous textures (also in BSE images, Fig. 6e). Biotite occurs as reddish-

273 brown tabular phenocrysts with subehdral to euhedral habits, and is normally associated with the other

274 crystalline phases (Fig. 6a, b). Magnetite are subehdral and sub-millimetric in size, and always display

275 exsolution textures (lamellae) in BSE images (Fig. 6f). Apatite inclusions have been observed within

276 plagioclase, amphibole and biotite phenocrysts.

277
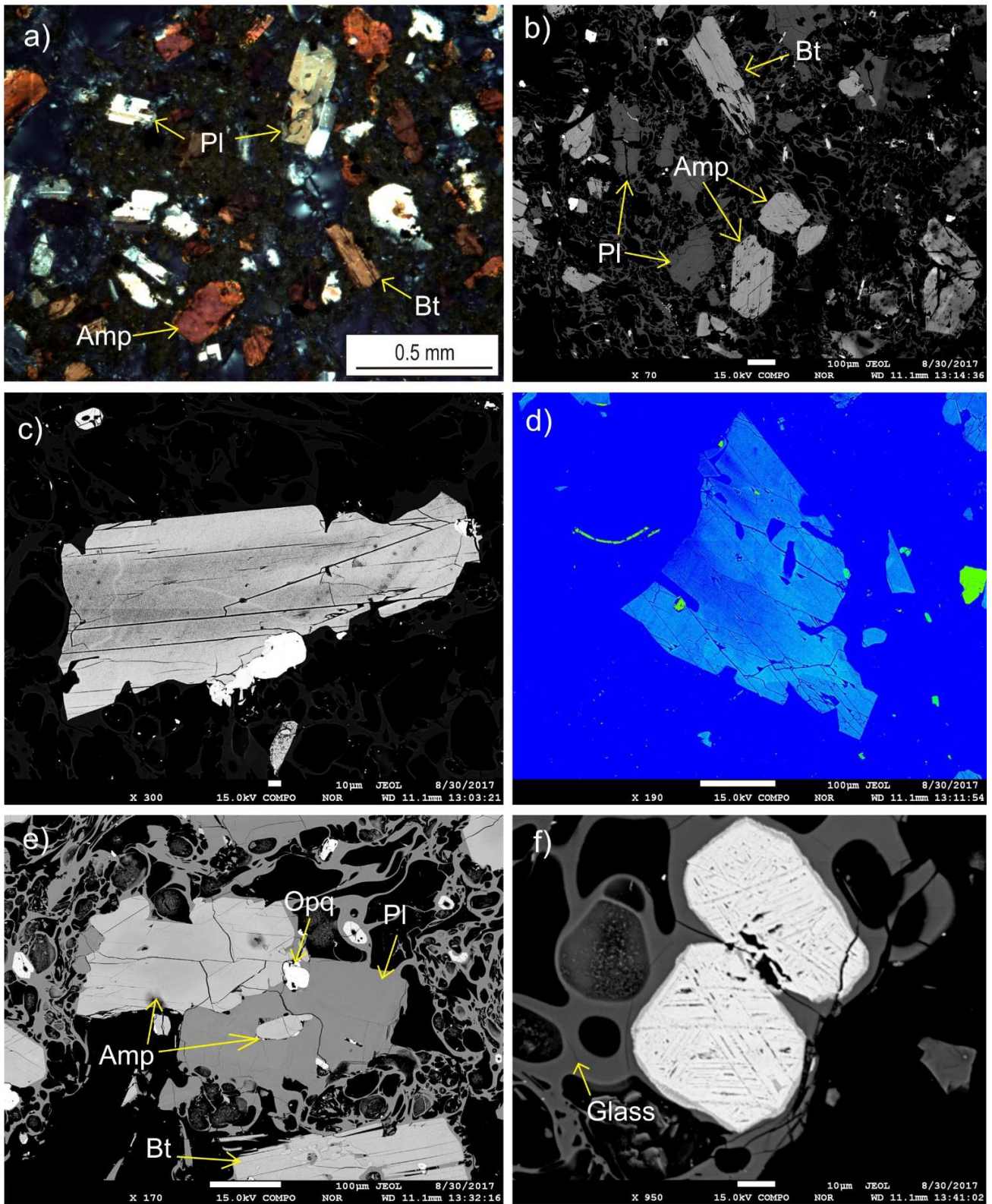
Figure 6. FBE petrographic features. a) Microphotograph (cross-polarized lights) showing the texture composed of Amp + Pl + Bt + Opq phenocrysts. b) Representative BSE image of FBE texture. c) Highly contrasted BSE image of an amphibole grain. d) Highly contrasted BSE color image of an amphibole crystal. e) BSE image of an amphibole and plagioclase

282 association and inclusion of amphibole within plagioclase; zoning in amphibole can be observed also with low-contrast BSE
283 images. f) BSE image of magnetite micro-phenocrysts showing exsolution lamellae texture.

284 *4.2.5. Coarse brown enclave (CBE)*

285 CBE displays seriate texture and a holohyaline vesiculated glass (Fig. 7a, b), with a mineral assemblage

286 constituted by Pl (35-40 %) + Bt (~25 %) + Amp (25 – 30 %) + Opq (5-10 %) + Ap (traces). P.I. is

287 about 20 % and the general crystal grainsize is coarser than FBE (Fig. 7a, b). Plagioclase exhibits

288 subehdral to euhedral tabular habits (0.5-1.5 mm) and displays both optical oscillatory and

289 homogeneous textures. Amphibole generally is present as isolated euhedral grains (~0.3-2 mm) and, to

290 a lesser extent, associated with the other crystalline phases (Fig. 7a-d). Core-rim zoning was not

291 observed at BSE imaging (Fig. 7c, d). Biotite occurs as reddish crystals with millimetric tabular

292 dimension (up to 2.5 mm). Opaque minerals are subehdral and sub-millimetric (~0.5 mm) and always

293 exhibit exolution texture (Fig. 7e). Apatite occur as inclusion within plagioclase, amphibole and biotite.

294 Crystal rich inclusions (Fig. 2h) display glomero-porphyritic texture and a mineral association

295 composed of Amp + Bt + minor Pl and Opq (P.I. ~40-60%) and a vesiculated glass (Figs. 7f, 7-A1 of

296 Supplementary Material). Commonly, the Amp + Bt aggregates surround cores of resorbed

297 orthopyroxene grains (Fig. 7f).
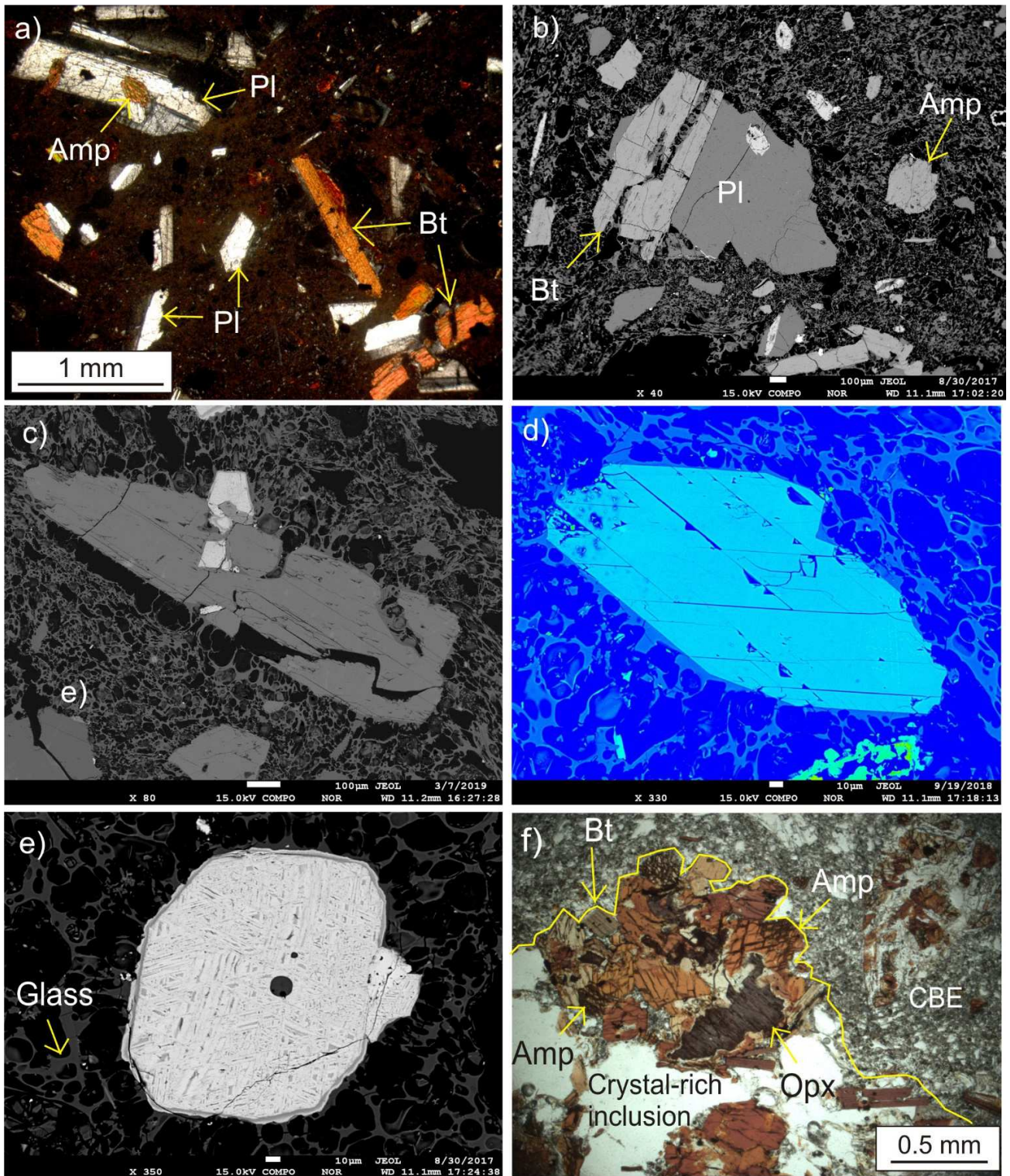
Figure 7. CBE petrographic features. a) Microphotograph (cross-polarized light) of the general texture. b) BSE image of the texture. c) BSE image of a millimetric amphibole crystal. d) High contrast BSE color image of an amphibole micro-phenocryst e) BSE image of a magnetite grain. f) Microphotograph (parallel-polarized light) of a crystal-rich inclusion showing the glomerocrystic association of Amp + Bt surrounding a resorbed Opx grain. Yellow outline highlights the limit between crystal-rich inclusion and CBE.

304 *4.3 Whole-rock, glass and mineral chemical composition*

305 We summarize in this section the main geochemical features of pumice samples and enclaves, together

306 with the composition of glass and mineral assemblages. The opaque mineral analyses will not be

307 described because of the general presence of exolution lamellae textures which invalidate the obtained

308 compositions. We provide the representative analyses in Tables 2 – 7 and the complete dataset in the

309 supplementary material (Tab. 8A).

310 *4.3.1. Whole-rock composition*

311 WP is metaluminous to slightly peraluminous rhyolite to trachydacite (Fig. 8a, b). A small decrease in

312 the SiO_2 content and alkalis ($Na_2O + K_2O$) from the lower part of the deposit (CPPI Phase I) towards

313 the top (CPPI Phase II) has been detected (from an average value of ca. 72 to 70 wt % of SiO_2, and

314 from 9 to 8 wt % of $Na_2O + K_2O$). WP Al_2O_3 abundance is comparable with BP and BE, and lower

315 than FBE and CBE (Fig. 8c). Contents of TiO_2, FeO, MgO and CaO in WP are lower, and K_2O is

316 higher than BP and all enclave types (Fig. 8d-h). WP zirconium contents are in the range of 155 – 214

317 ppm (Tabs. 2, 8A-1). BP displays metaluminous trachydacitic composition, and shows a slight

318 increment in the sum of alkalis with SiO_2 (Fig. 8a, b). In the binary plot of TiO_2, FeO, MgO, CaO and

319 K_2O versus SiO_2 contents, BP composition always plots in intermediate positions respect those of WP

320 and the enclaves (Fig. 8c-h). BE is a basaltic trachyandesite with metaluminous affinity (Fig. 8a, b).

321 Among the enclaves, it displays the highest MgO and the lowest TiO_2 and Al_2O_3 contents (Fig. 8c-e),

322 while FeO and CaO abundance is similar to FBE and CBE (Fig. 8f, g), which are a basaltic

323 trachyandesites with metaluminous affinity (Fig. 8a, b) and differences in the SiO_2 abundance (Fig. 8a-

324 h). In the FeO/MgO ratio versus 1/MgO diagram (whole rock), two different linear relations can be

325 observed among BE, FBE and CBE, and BE, BP and WP facies (Fig. 8i).
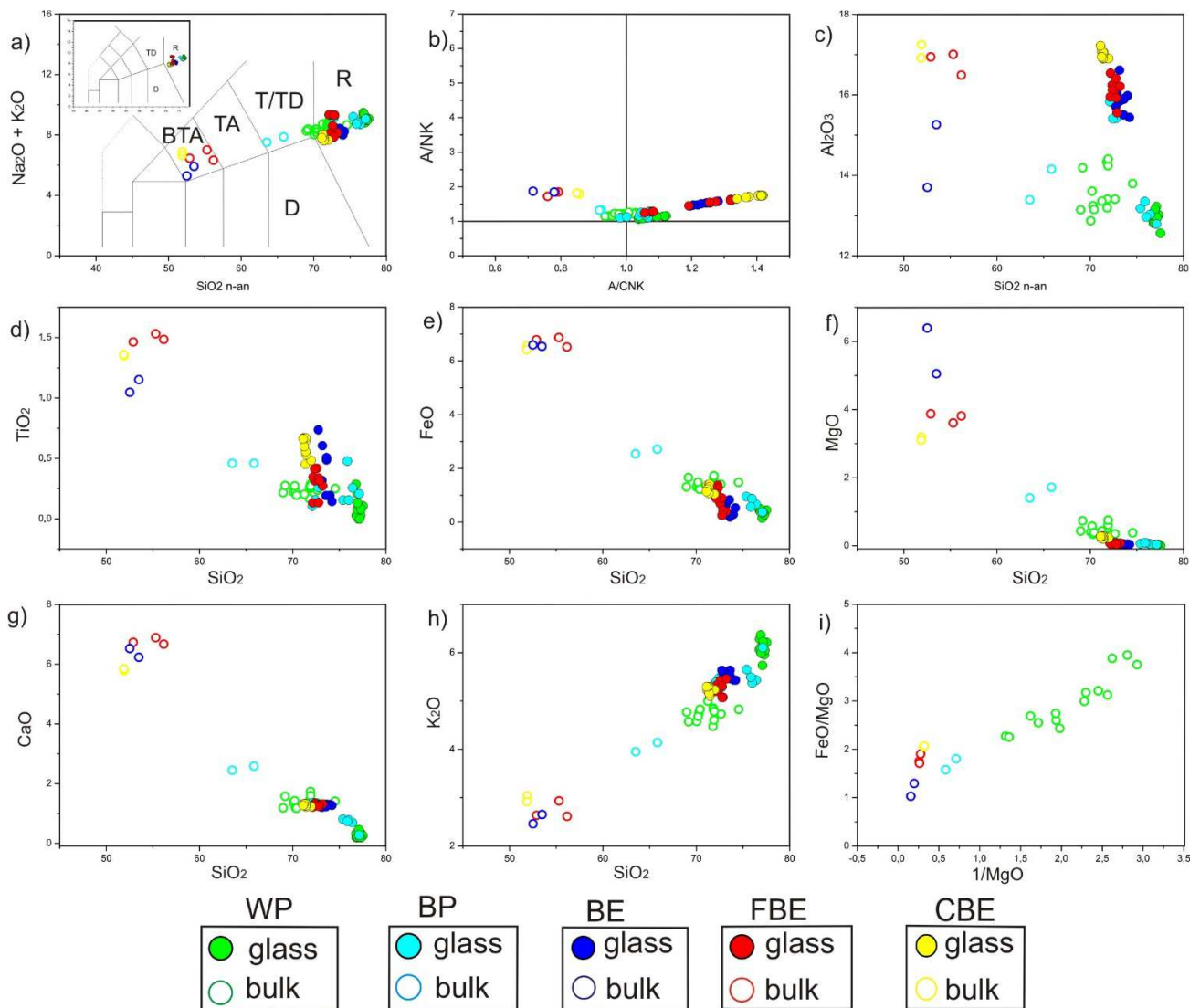
Figure 8. a) TAS (Le Bas et al., 1986) classification of the CPPI whole rock and glass; letters indicate the TAS fields: T/TD = trachyte/trachydacite; D = dacite; R = rhyolite. Right inset shows the entire TAS diagram. b) ASI (Alumina Saturation Index) of the CPPI sample glass. c) Binary diagram of Al_2O_3 versus SiO_2. d) Binary diagram of TiO_2 versus SiO_2. e) Binary diagram of FeO versus SiO_2. f) Binary diagram of MgO versus SiO_2. g) Binary diagram of CaO versus SiO_2. h) Binary diagram of K_2O versus SiO_2. i) Binary diagram of FeO/MgO versus 1/MgO. Oxides are expressed as wt %.

4.3.2. Glass

WP glass displays high-silica, slightly peraluminous composition (Fig. 8a,b) with the lowest contents of Al_2O_3, MgO and CaO (Fig. 8 c, f, g) and highest K_2O contents of the entire dataset (Fig. 8c, f, g). The BP-glass major oxide contents display the highest variability among the analyzed samples, showing affinity with both WP and the enclave glass composition (mostly with BE and FBE analyses; Fig. 8c-i).

338   Glass in the enclaves is peraluminous and rhyolitic. The BE glass displays the most evolved

339   composition (Fig. 8a), while the CBE is the least evolved and the FBE is intermediate (in terms of

340   silica abundance). The three enclave types have similar contents of CaO (Fig. 8g), while relative

341   differences exist in the other oxides. Al_2O_3 and MgO contents are higher in CBE than in FBE and BE

342   (Fig. 8c, f), as well as FeO and TiO_2, for which a partial overlap exists between CBE and FBE and

343   between CBE and BE respectively (Fig. 8d, e).

344   Tables 2, 3

345   *4.3.3. Feldspars*

346   The general range of the CPPI plagioclase composition spans from oligoclase to bytownite, being

347   andesine and labradorite the most abundant species (Fig. 9). WP homogeneous plagioclase grains vary

348   from oligoclase to andesine (An_{21-30}; Fig. 10a), and the optically-oscillatory zoned crystals (Fig. 9b)

349   reach more anorthitic compositions in the brighter areas (An_{30-59}; Fig. 9a). Plagioclase in BP is similar

350   to WP oscillatory-zoned grains, displaying general andesine composition (An_{31-44}; Fig. 9a). BE

351   plagioclase compositions are the most heterogeneous among the analyzed rocks, spanning from

352   andesine to bytownite (Fig. 9c). Groundmass microlites (Fig. 4a,b) and anhedral grains (Fig. 4e) vary

353   from andesine to bytownite (An_{38-82} and An_{27-83} respectively; Fig. 9c; Table 3, 14), the plagioclase

354   phenocrysts (Fig. 5g) have high anorthite cores (An_{74-83}) and lesser calcic rims (An_{64-77}), while sieve-

355   textured grains (Fig. 5i) vary between An_{30-51} (cores) and An_{30-47} (rims), similarly to plagioclase

356   composition of WP and BP samples (Fig. 9a, c). FBE and CBE plagioclase are similar (An_{38-55} and

357   An_{41-57} respectively; Fig. 9d) with the former showing general less anorthitic composition (average

358   ~An_{46}) than the latter (~An_{52}). Core-rim variations indicate no zoning or slightly normal zoning for

359   FBE plagioclases (average An_{48} and An_{47} for core and rim respectively; Fig. 9d), and normal zoning for

360   CBE (average An_{55} and An_{46} for core and rim respectively; Fig. 9d).

361   Analyzed K-feldspar grains display homogeneous composition in all rock in which are contained (WP,

362   BP, and BE). They are sanidine with a structural formula of Or_{69-72} Ab_{26-29} An_{0-1} (Fig. 9a, c).

363
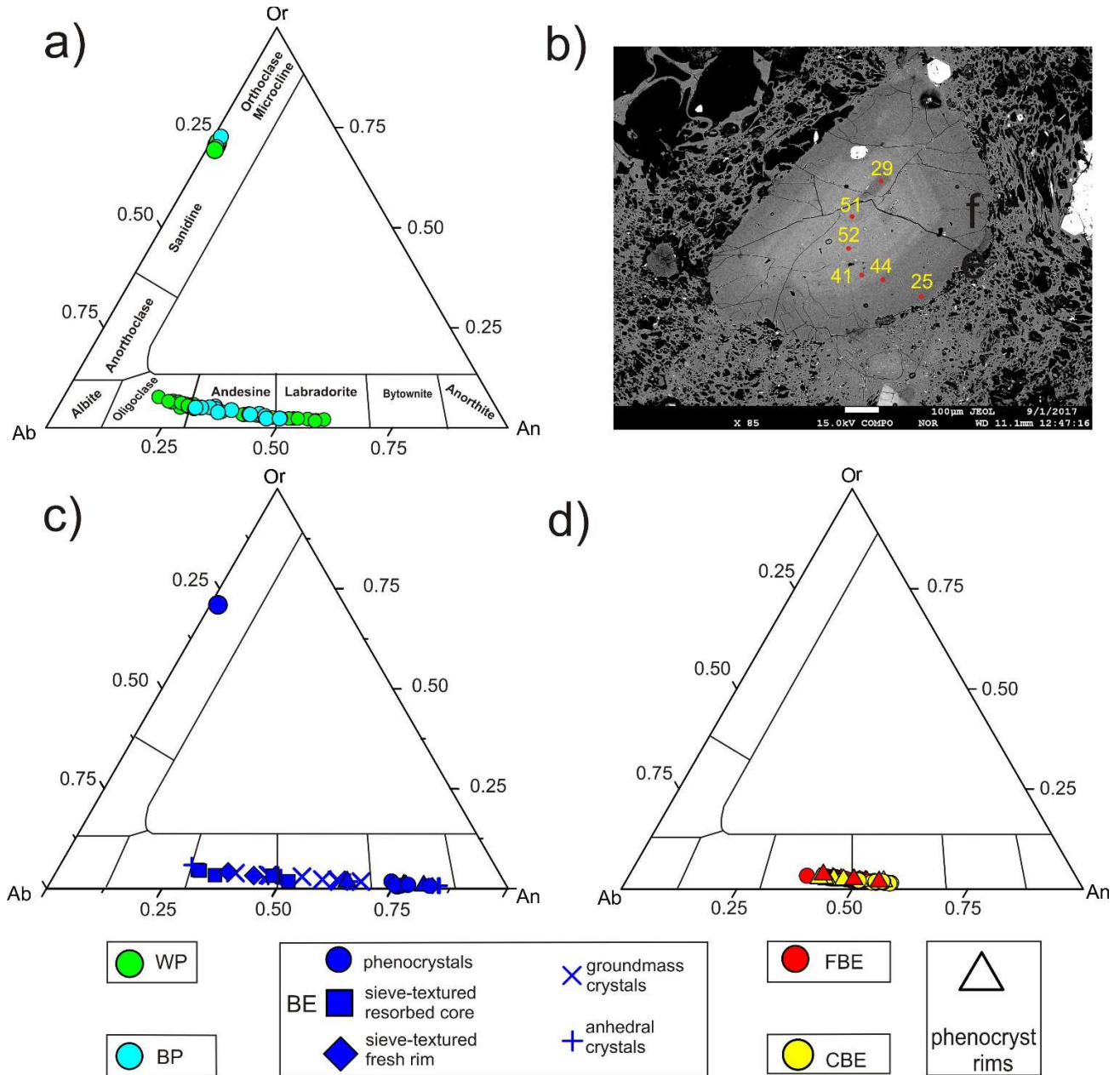
Figure 9. Classification of CPPI feldspars in An (anorthite) - Ab (Albite) - Or (orthoclase) ternary diagrams. a) WP and
BP plagioclase composition. b) BSE image of an oscillatory-zone plagioclase phenocryst of WP; yellow numbers indicate
the calculated anorthite contents. c) BE plagioclase composition. d) FBE and CBE plagioclase composition. WP and BP
analyses are not divided into core and rim because most point analyses represent the oscillatory-zoned grains (Fig. 3 c-d;
see text for details).

369   Table 4

370   *4.3.4. Biotite*

371 All biotite grains from pumice and enclaves plot in the annite field in the classification diagram of

372 Clarke (1981) and in the calc-alkaline field of the classification of Abdel-Rahman (1994, Fig. 10a, b).

373 WP, BP and BE biotite grains show similar compositions (Fig. 10a-d). They differ from FBE and CBE

374 in terms of Al$^{[IV]}$ (apfu), Fe# (Fe/(Fe + Mg), and wt % of SiO_2, FeO and MgO (Fig. 10a-d), while Ti

375 contents are comparable (Fig. 10c). Biotite phenocrysts from FBE and CBE slightly differ in MgO,

376 FeO and Al$^{[IV]}$ contents (Fig. 10 a-d).
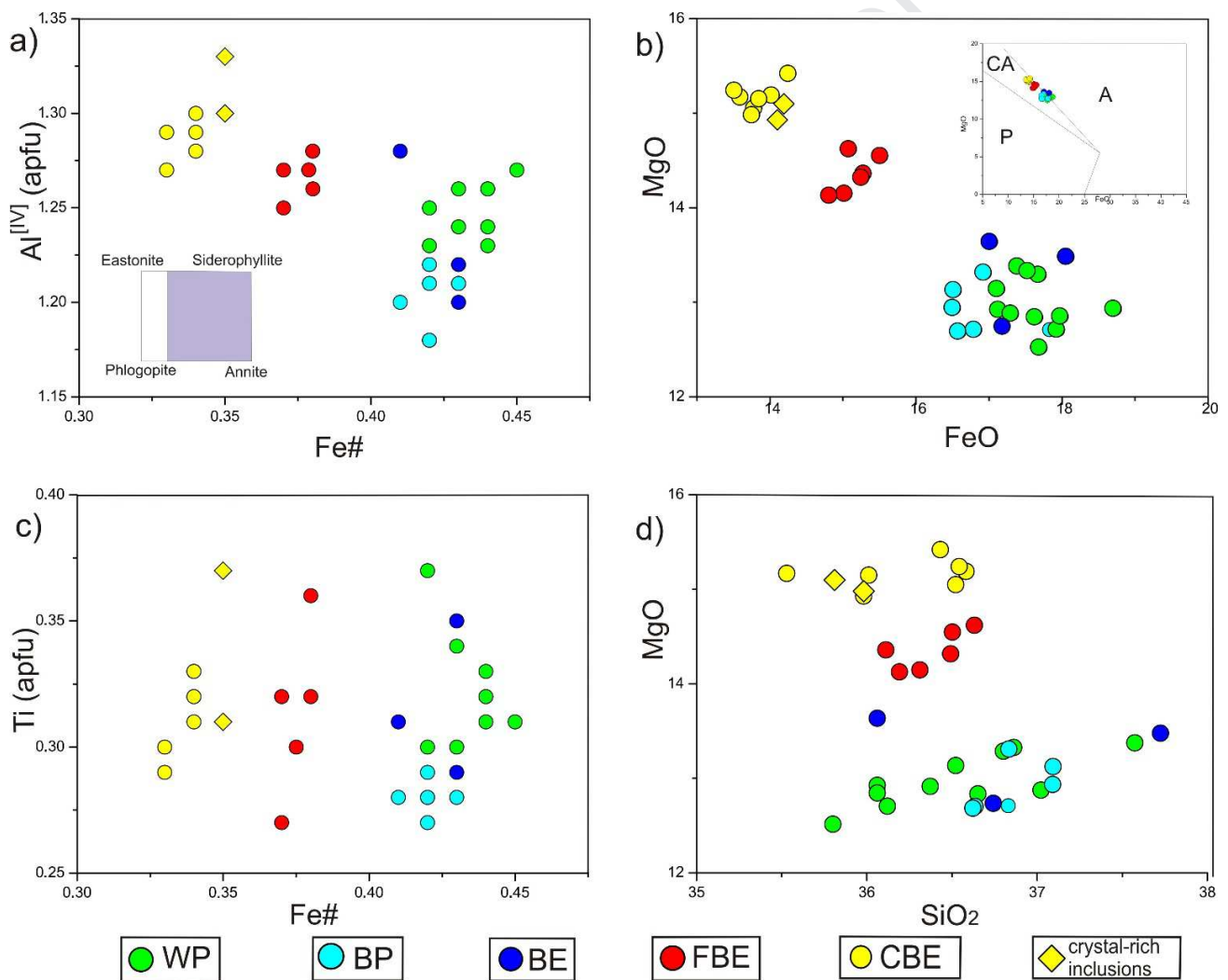
378 Figure 10. a) CPPI biotite classification of Clarke (1981); left inset showing the compositional fields. b) Biotite
379 classification of Abdel Rahman (1994). The right inset indicates the compositional fields: CA = calcalkaline; P =
380 peraluminous; A = alkaline. c) Ti (atom per formula unit) versus Fe# (Fe/Fe + Mg) diagram. d) Binary diagram of MgO
381 versus SiO_2. Oxides are expressed as wt %.

382   *4.3.6. Pyroxenes*

383   WP clinopyroxene plots in the limit between augite and diopside fields (classification of Morimoto

384   1988) showing a more ferric character (Wo_{46-47} En_{37-38} FS_{18-20}) and lower Mg# (~0.68-0.71; Tab. 5)

385   than clinopyroxene from BE, which display augitic composition (structural formula Wo_{41-44} En_{41-47}

386   Fs_{12-18} with one sample Wo_{37} En_{49} Fs_{16}, Fig. 11a), and higher Mg# (~0.73-0.81). Within BP,

387   clinopyroxene is also augite (n =1 analysis), and display identical structural formula of BE phenocrysts

388   (Wo_{43} En_{44} Fs_{14}) and Mg# (0.77; Tab. 5), which was predictable considering the similar textural

389   features of BE phenocrysts and BP clinopyroxene grains (Fig. 4c-d; Fig. 5a).

390   All analyzed orthopyroxene grains fall in the enstatite field according to Morimoto (1988)

391   classification (Fig. 11a). Grains within WP display similar structural formula (Wo_{1-2} En_{76-78} Fs_{20-21}) and

392   Mg# (0.78-0.79) to BE phenocrysts (Wo_{2-3} En_{74-79} Fs_{17-22}; Mg# = 0.76-0.81) and large phenocrysts

393   (Wo_2 En_{78} Fs_{19}; Mg# = 0.80). Differently, BP orthopyroxenes are more ferric in composition (Wo_{2-3}

394   En_{70-74} Fs_{22-30}) and exhibit lower Mg# (0.73-0.77) than crystals from WP and BE (Fig. 11a, b),

395   similarly to orthopyroxene resorbed cores within CBE crystal-rich inclusions (Wo_3 En_{66-70} Fs_{26-30}; Mg#

396   = 0.68-0.72; Figs. 7g, h; 11).

397   Table 5

398   *4.3.7. Olivine*

399   Olivine phenocrysts composition in BE (and olivine inclusion within the large amphibole phenocryst;

400   Fig. 5k) varies from Fo_{69-78}, and similar compositions were calculated for the olivine grains in WP and

401   BP samples (Fo_{75} and Fo_{77} respectively; Table 6).

402
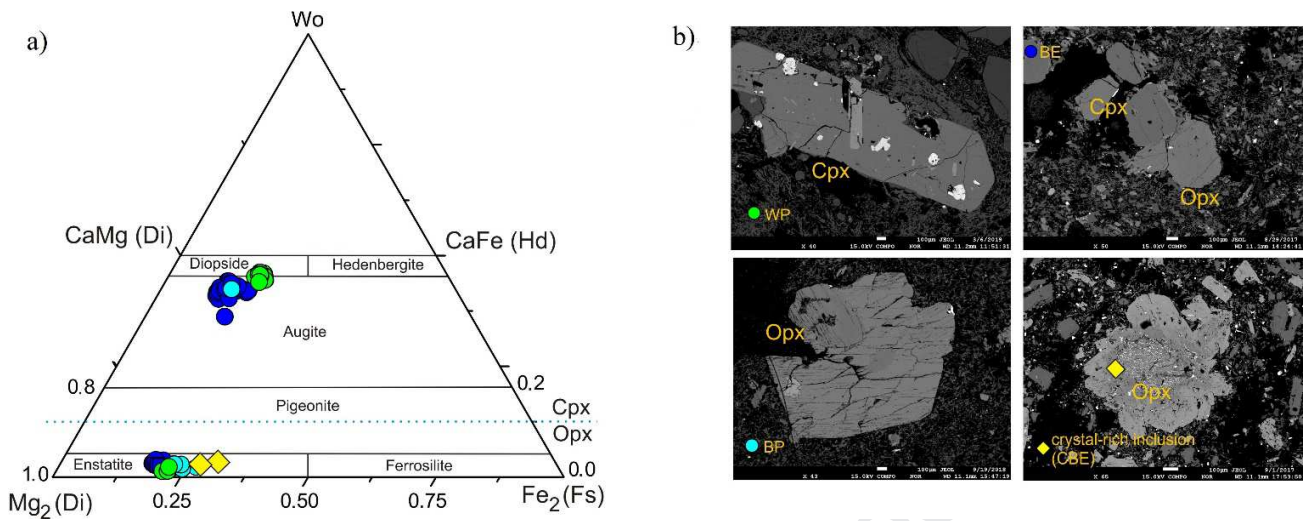
403 Figure 11. a) Ternary pyroxene classification of the CPPI pyroxenes from Morimoto (1988). Wo= wollastonite; En =
404 enstatite; Fs= ferrosilite. Blu squares indicate BE orthopyroxene large phenocrysts (Fig. 5-A1 of Supplementary Material. b)
405 graphic legend with a clinopyroxene phenocryst of WP (upper left, Fig. 3e), a clinopyroxene-orthopyroxene aggregate
406 within BE (upper right; e.g. Fig. 5a), an orthopyroxene associated to amphibole within BP (lower left, e.g. Fig. 3g), and a
407 resorbed orthopyroxene core surrounded by amphibole and biotite within the CBE crystal-rich inclusions (e.g. Fig. 7f).

408 Table 5

409 *4.3.8. Amphibole*

410 Amphibole cationic abundances were calculated according to the default method of Ridolfi et al.

411 (2018), and mineral formula was determined with the Locok (2014) and Ridolfi et al. (2018) methods;

412 only one sample (106A-C4-Anf1-ccl) needed minor correction for the formula and cationic abundances

413 calculations. All amphibole grains belong to the W (OH, F, Cl) - dominated group, Ca subgroup

414 (Ridolfi et al., 2018), and classify, according to Locock et al. (2014), as Ti-rich pargasite (n = 46), Ti-

415 rich magnesio-hastingite (n = 17), rootname4 (n = 15) magnesio-hastingite (n = 9) and minor pargasite

416 (n = 3), Ti-rich ferri-sadanagaite (n = 1), and ferri-rootname4 (n = 2). FBE amphiboles display a wider

417 range in the cations Si, Ti, Al$^{[IV]}$ (apfu) and Mg# than CBE (Fig. 12a,b) with cores being more enriched

418 in Ti and depleted in Si than rims. Mg# is rather homogeneous, with average values of 0.70 and 0.67

419 respectively for core and rim amphibole areas (Fig. 12a, b). CBE grains (core and rim) are more similar

420 to FBE cores in terms of Ti, Si, Al$^{[IV]}$ and also in Mg# (average 0.70) than FBE rims (Fig. 12a, b).

421 Within BE, groundmass microlites display lower Mg# and comparable (Na+Ca)$_A$ than the corona-

422   forming microcrystals (Fig. 12 c), while the other parameters (Si, Ti, $Al^{[IV]}$) are comparable (Fig. 12a,

423   b). Amphibole large phenocrysts (Fig 5k) differ from BE, FBE and CBE amphiboles in having higher

424   Mg# and lower Ti contents (Fig. 12a, b).
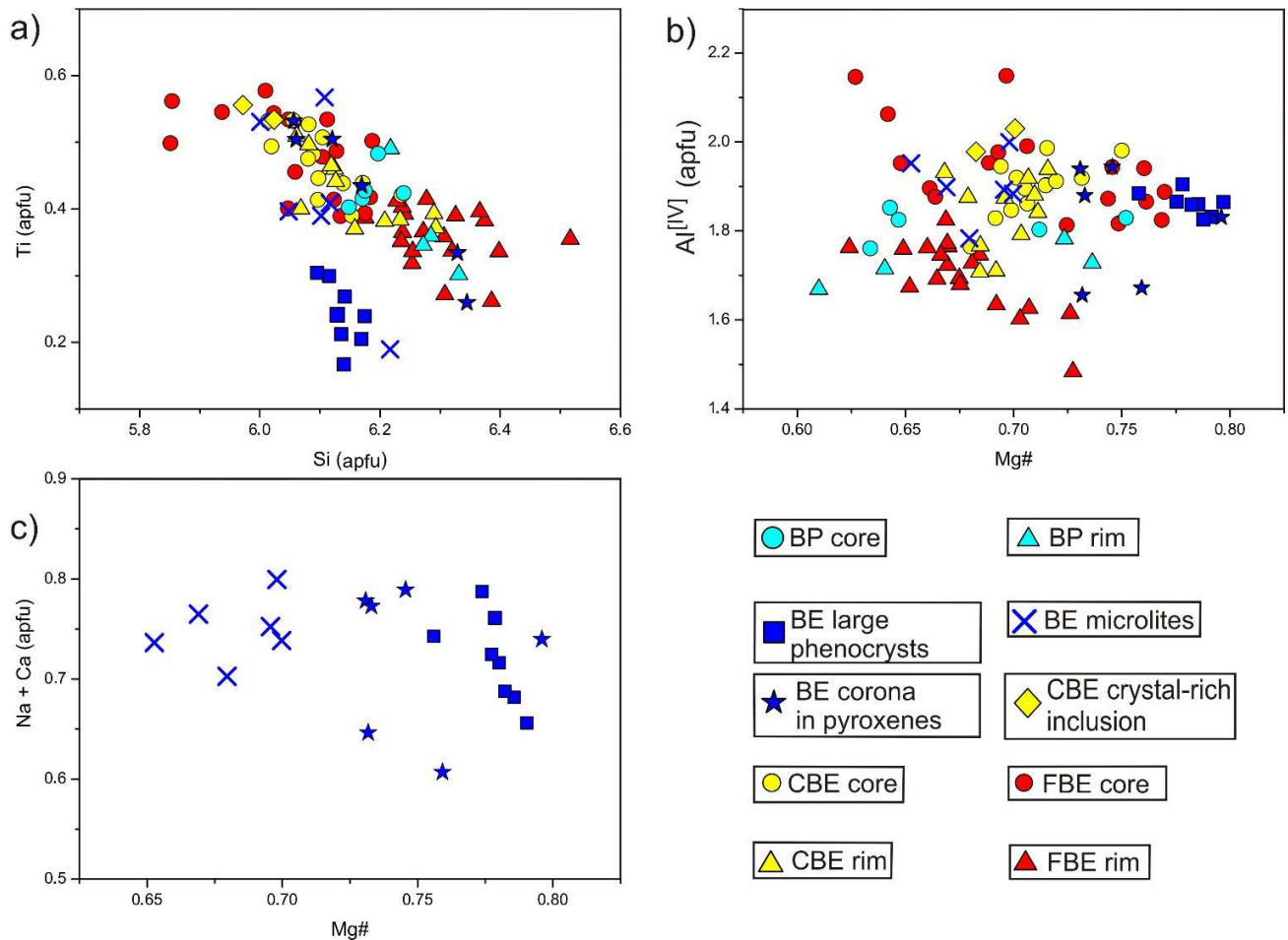
425

426   Figure 12. a) Binary diagram of cationic Ti (apfu) versus Si (apfu) for all the analyzed amphibole grains. b) Binary diagram
427   showing cationic $Al^{[IV]}$ (apfu) versus Mg# (Mg/(Mg + Fe^{2+})). c) Binary diagram showing the sum of apfu Na + Ca (A-site)
428   versus Mg#.

429   Table 7

430   **5. Thermobarometry and hygrometry**

431   In order to define the physical conditions (T, P, H_2O^{liq} contents) of the magmas that form the CPPI

432   magmatic system and to disclose the possible depth at which the rhyolitic and enclave-forming magmas

433   interacted, we realized a suite of themobarometric calculations, following the workflow proposed by

434   Lucci et al. (2020). Results from the thermobarometric modelling are then presented and discussed

435   following a statistical approach (e.g. Calzolari et al., 2018; Lucci et al., 2020).

5.1. General considerations

437   We integrate a suite of mineral-liquid, mineral-mineral and single mineral thermobarometry models

438   such as (i) olivine-liquid (Putirka, 2008), (ii) clinopyroxene-liquid (Putirka, 2008), (iii) orthopyroxene-

439   liquid (Putirka, 2008), (iv) plagioclase-liquid (Putirka, 2005, 2008), (v) plagioclase-alkali feldspar

440   (Putirka, 2008), (vi) clinopyroxene-orthopyroxene (Putirka, 2008), (vii) amphibole chemistry (Ridolfi

441   and Renzulli, 2012) models. For mineral-liquid models we used both glass and bulk rock composition

442   as input, while for the clinopyroxene-orthopyroxene thermobarometric calculations touching pairs (Fig.

443   8A-6) were used and combined with analyses of sparse crystals. The equilibrium plagioclase-liquid

444   pairs used in the T, P and H_2O^{liq} estimations were selected after the application of the filter model

445   proposed by Putirka (2008): $(K_D^{pl-liq}(An-Ab) = 0.1 \pm 0.05$ for T < 1050 °C and = 0.27 ± 0.11 for T >

446   1050 °C), followed by the test proposed by Namur et al. (2012), which compares the measured

447   anorthite fraction of plagioclase and that calculated for the liquid composition. The pairs that satisfy the

448   test are those with an $An_{measured}/An_{calculated}$ ratio of 1.0 ± 0.1 (Fig. 13). The values of $H2O^{liq}$ (wt % of

449   water in the nominal melt) obtained from the plagioclase-liquid model (equation 25b of Putirka, 2008)

450   were used as input for the clinopyroxene-liquid equations, and compared with the amphibole

451   hygrometer of Ridolfi and Renzulli (2012). The equilibrium clinopyroxene-liquid, orthopyroxene-

452   liquid, olivine-liquid, and two-pyroxene compositional pairs were selected through the equilibrium test

453   proposed by Putirka (2008) for each model $(K_D^{cpx-liq}(Fe-Mg) = 0.28 \pm 0.7$; $K_D^{opx-liq}(Fe-Mg) = .0.29 \pm$

454   0.6; $K_D^{ol-liq}(Fe-Mg) = .0.30 \pm 0.3$; $K_D^{cpx-opx}(Fe-Mg) = .1.09 \pm 0.14$, respectively). The graphical

455   representation of these equilibrium test (binary diagrams of mineral Mg# versus liquid Mg#; e.g. Risse

456   et al., 2013; Lucci et al., 2020) are provided in the Fugure 8-A7 of the Supplementary Material. For the

457   two-feldspars model we consider the equilibrium test proposed by Elkins and Grove (1990), which

458   considers the relative ratio of the activities of the distinct feldspars components (An, Ab, Or) between

459   plagioclase and K-feldspar crystal pairs (the ratio should be nominally = 0). The input pressure values

460   used for the two-feldspars model were obtained from barometric estimation obtained for

461   clinopyroxene-liquid and plagioclase-liquid for WP. We also calculated the zircon saturation

462   temperatures from the model of Watson and Harrison, (1983), using the Zr content (ppm) of WP

463   samples (Tab. 2). Results (T, P, H_2O wt %) are provided in Figure 14 and Table 9A of the

464   Supplementary Material, except for those from the amphibole composition method that are shown

465   together within the EPMA analysis in Table 6.

466
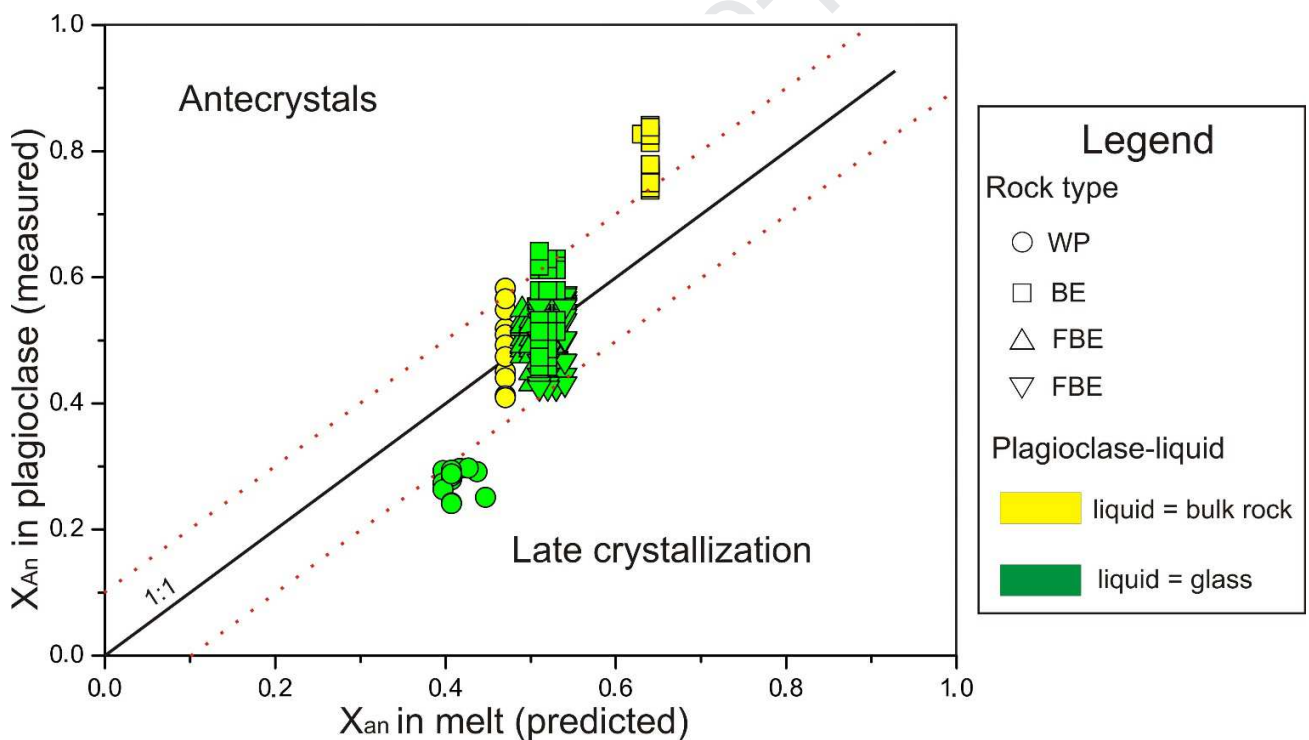
467   Fig. 13. Binary plot of the measured plagioclase anorthite fraction versus that calculated from the liquid composition by the
468   method of Namur et al. (2012), applied to the plagioclase-liquid pairs that satisfied the equilibrium test of Putirka (2008;
469   Tab. 8A-3). Equilibrium WP plagioclase-liquid pairs are those obtained combining the high anorthite areas of oscillatory
470   plagioclase with bulk-rock compositions.

471   *5.2. Hygrometric estimates*

472   The values of H_2O^{liq} obtained by the plagioclase-liquid and amphibole hygrometer ($\pm$ 1σ standard

473   deviation of the weighted mean) are provided as isolines in the P-T diagram of Figure 14. WP

474   calculated H_2O wt % was determined by equilibrium plagioclase + bulk-rock compositions (Fig. 13)

475   and varies between ~ 0.89-1.32 wt % (weighted mean of 1.17 $\pm$ 0.49, MSWD = 0.021; n = 15). In BE

476   samples, water contents were determined using the compositions of the plagioclase microlites (Figs. 5b,

477   c; 9c) paired with EPMA glass analyses (Fig. 13). The obtained H_2O range is between 1.2-1.42 wt %

478   (weighted mean of 1.28 $\pm$ 0.42 wt %, MSWD = 0.042, n = 11). For FBE the plagioclase-liquid model

479   provides water contents of 0.98-1.59 wt % (weighted mean of 1.38 $\pm$0.25 wt %, MSWD = 0.013, n =

480   67), similar to CBE (0.89-1.46 wt %, weighted mean = 1.30 $\pm$ 0.17 wt %, MSWD = 0.008, n =144).

481   For BP samples the equilibrium test of Putirka (2008) was not satisfied, either using bulk rock and

482   glass composition, and results will not be discussed. The application of the amphibole hygrometer

483   provides, for all the enclave types, higher water contents than the plagioclase-liquid method, with FBE

484   and CBE varying between ~ 4-6 wt % and the BE large phenocrysts displaying the highest H_2O^{liq} range

485   (~ 8 – 10 wt %).

486   *5.3. Thermobarometric estimates*

487   We provide in this section the results obtained for each rock by the equilibrium mineral-liquid and

488   mineral-mineral pairs, together with those from the amphibole composition and zircon saturation

489   methods.

490   *5.3.1. White pumice*

491   The plagioclase-liquid thermobarometric model (using WP bulk rock composition as liquid input, n =

492   15; Fig. 13) provides a temperature range of 955-971 °C (weighted mean of 962 $\pm$ 22 °C, MSWD =

493   0.014) and a pressure range between 1.3 – 4.0 Kbar (weighted mean of 2.7 $\pm$ 1.3, MSWD = 0.13),

494   using equation 24a and 25a of Putirka (2005), respectively. The unique plagioclase-liquid pairs that

495 satisfied the equilibrium test of Putirka, (2008) are those obtained using the high-An compositions of

496 oscillatory plagioclase phenocrysts (Figs. 9a, b; 13). The clinopyroxene-liquid (whole rock) model of

497 Putirka (2008) yields a temperature range ~ 883-930 °C (weighted mean of 906 ± 9 °C, MSWD =

498 0.056, n =119), and a pressure of 1.8 – 4.2 Kbar, (weighted mean of 2.6 ± 0.6, MSWD = 0.031). The

499 two-feldspars thermometer provided a lower and wider temperature range than the clinopyroxene- and

500 plagioclase-liquid models (810 – 929 °C, weighted mean of 893 ± 13 °C, MSWD = 0.113, n = 43). The

501 plagioclase – K-feldspar pairs were chosen among those with a calculated An-Ab-Or activity difference

502 in the feldspars pairs < 0.1 (Table 8A-2). The pairs that resulted in equilibrium are those formed by the

503 WP low-An phenocrysts and the low-An areas of oscillatory grains (Fig. 9a, b). Finally, the zircon

504 saturation temperatures are in the range ~ 780-800 °C (weighted mean = 788 ± 15 °C, MSWD = 0.059,

505 n = 16; Tables. 2, 8A-1).

506 *5.3.2. Beige pumice*

507 Temperature and pressure estimates for BP were determined by the amphibole composition model

508 (Ridolfi and Renzulli, 2012), which yielded a temperature range of 921-991 °C, (average 946 ± 45 °C,

509 n = 4) and 966-981 °C (average 969 ± 45 °C, n = 5) for amphibole rim and core, respectively. Pressure

510 estimates are in the range of 2.4 – 4.4 Kbar, average 3.35 ± 0.48 Kbar and 2.9 – 4.3 Kbar, average 3.5

511 ± 0.48 for rims and cores, respectively.

512 *5.3.3. Black enclave*

513 Temperatures and pressure values for BE were calculated using the olivine-liquid, orthopyroxene-

514 liquid, the clinopyroxene-liquid (all using BE bulk rock composition), the plagioclase – liquid (using

515 microlite – glass pairs), the two-pyroxenes and the amphibole composition methods (Fig.14). The

516 equilibrium olivine-liquid pairs (n = 2) yielded temperatures of 1171-1175 °C (± 52 ° C; eq. 2 of

517 Putirka et al., 2007; Tab. 9A-5), the orthopyroxene-liquid model provided a temperature range of 1099

518   – 1131 °C (weighted mean of 1119 ± 18 °C, MSWD = 0.044, n = 19), and a pressure range between 5.7

519   – 8.5 Kbar (weighted mean = 7.1 ± 1.2, MSWD = 0.112), and the clinopyroxen-liquid equilibrium pairs

520   yielded a temperature range of 1140-1159 °C (weighted mean = 1147 ± 21 °C, MSWD = 0.019) and a

521   pressure range of 5.4-7.8 Kbar (weigted mean = 6.8 ± 1.7, MSWD = 0.055). The two-pyroxenes

522   thermobarometer provided lower temperature and pressure ranges (955 – 1016 °C, weighted mean of

523   992 ± 5.6 °C, MSWD = 0.13, n = 259), and 1.1 – 6.2 Kbar (weighted mean of 3.0 ± 0.35 Kbar, MSWD

524   = 0.15). The large amphibole phenocrysts (Fig. 5k) yielded a temperature range of 950 – 996 °C

525   (average 973 ± 45 °C, n = 7), and a pressure range of 8.1 – 9.0 Kbar (average 8.51 ± 1.44 Kbar). The

526   Ridolfi and Renzulli (2012) was not applied to BE amphiboles microlithes, which are not suitable for

527   the above-mentioned model (Ridolfi et al., 2010).

528

529   *5.3.4. Fine brown enclave*

530   Temperature and pressure estimates for FBE were realized using the plagioclase-liquid (with

531   plagioclase-glass pairs; Fig. 13) and the amphibole composition methods. FBE amphiboles are

532   prismatic to tabular and are not mircolites (0.25-1.5 mm) in contrast to the BE amphiboles (Fig.5 b, c).

533   The plagioclase-liquid temperature estimates are in the range ~ 970-980 °C (weighted mean of 975 ±

534   11 °C, MSWD = 0.0042, n = 67), while pressure is between 1.0 - 5.3 Kbar (weighted mean of 3.42 ±

535   0.6 Kbar, MSWD = 0.13). FBE amphibole core analyses yielded temperatures between 981 – 1023 °C

536   (weighted mean of 1000 ± 22, MSWD = 0.087, n = 17), and pressure in the range 4.1 – 7.8 Kbar

537   (weighted mean of 5.8 ± 0.64, MSWD = 1.9), and the amphibole rims provided lower temperature (

538   914 – 943 °C, weighted mean of 933 ± 21, MSWD = 0.088, n = 19), and pressure ranges (2.5 – 3.3

539   Kbar, weighted mean of 2.88 ± 0.17, MSWD = 0.994).

540   *5.3.5. Coarse brown enclave*

541 As well as FBE, CBE temperature and pressure estimates were realized with the plagioclase-glass pairs

542 and with amphibole compositions. The first method yielded temperature in the range 978 – 1000 °C

543 (weighted mean of 989 ± 7 °C, MSWD = 0.073, n = 144), and pressures between 0 – 3.1 Kbar

544 (weighted mean of 1.8 ± 0.4 Kbar, MSWD = 0.047). In contrast to FBE, CBE core and rim analyses do

545 not form two distinct T-P groups (Fig. 14), providing temperatures in the range 968 – 1035 °C

546 (weighted mean of 1000 ± 25, MSWD = 0.993, n = 13) and between 966 – 1029 °C (weighted mean =

547 1005 ± 25 °C, MSWD = 0.2, n = 13), respectively. Also the estimated pressure is more variable than

548 FBE amphible (3.1 – 7.0 Kbar, weighted mean = 5.88 ± 0.88 Kbar), and between 3.0 -7.6 Kbar

549 (weighted mean of 5.4 ± 1.0 Kbar, MSWD = 3.5) for core and rims, respectively.
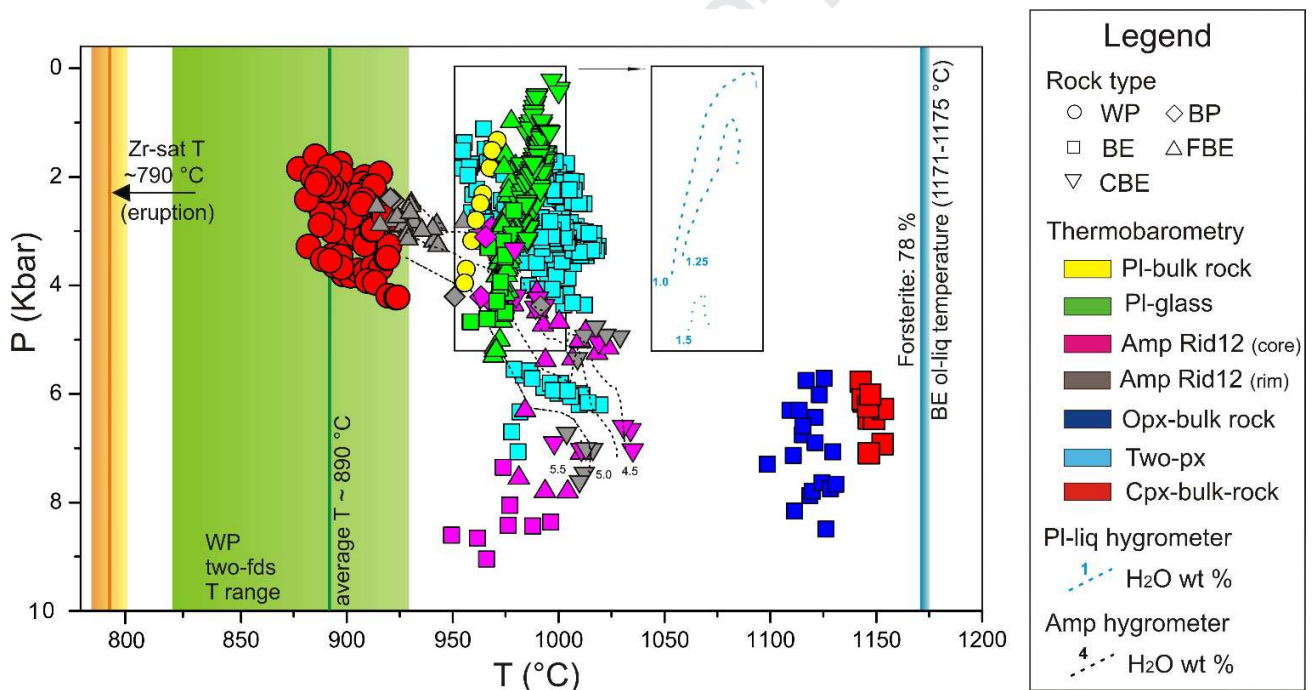
551 Fig. 14. Thermobarometric results. Pressure versus Temperature diagram. Symbols indicate the rock types, while colors are
552 associated to the applied thermobarometric models. Shaded light blue, green and orange areas indicate, respectively, the
553 calculated olivine-liquid, two-feldspars and zircon-saturation temperature ranges. Plagioclase-liquid hygrometer H_2O
554 isolines are provided translated in the central box to uncover them from the symbol cloud.

555

6. Discussion

557 *6.1. Petrologic and textural evidence of magmatic interaction*

558   The results of our study indicate that the complex petrologic characteristics of the CPPI products reflect

559   variable degrees of interaction (chemical and physical) between the rhyolite and the enclave-forming

560   magmas. The simplified model of Figure 15 resumes our reconstruction of the pre-eruptive stages of

561   the CPPI magmatic system. According to our interpretation, during the mafic recharge phase, mingling

562   between mafic and rhyolitic magmas was very intense, and partial hybridization of the rhyolitic host

563   (i.e. magma mixing) occurred. Mingling is normally associated with magmas with different

564   compositions, temperatures and rheology, which cannot mix completely to form hybrid products (Blake

565   and Fink, 2000). The intense mingling, evidenced by the composition and structure of the multi-banded

566   pumice (Fig. 2h, g), is also reflected in the complex mineralogical assemblages and micro-textures of

567   the enclaves and silicic pumice, suggesting that this interaction acted at different scales (e.g. Perugini

568   and Poli, 2012). Among the enclaves, BE is that displays greater textural and compositional evidence

569   of interaction with WP, occurring as partially dismembered inclusions within WP (Fig. 2c; Fig. 15a-3),

570   and showing the occurrence of crystal transfer to and from WP melt (Figs. 5h-j; 5-A2; 15a-1). This

571   suggests that the BE and WP magma exchanged crystals and melt components (micro-mingling

572   textures), as well as heat and volatiles (e.g. Huppert et al., 1982; Shane et al., 2008; Perugini and Poli,

573   2012; Scruggs and Putirka, 2018). Moreover, the variability on BE plagioclase composition and

574   textures (Figs. 6g-i; 9c), the silicic sieve-textured plagioclase within BE (Fig. 6h), and the presence of

575   amphibole rims on BE mafic phenocrysts (Fig. 5e, f), are features associated with magma mixing

576   events (Leonard et al., 2002; Coombs et al., 2003; Coombs and Gardner; 2004; de Hoog et al., 2004;

577   Ruprecht and Wörner, 2007; Humphreys et al., 2009; Gogoi and Saikia, 2018). By consequence, it is

578   likely that the generation of hybrid products may have occurred during the initial phase of BE-magma

579   injection (i.e. before quenching), during which mafic magma engulfed some rhyolitic crystal and melts

580   and generated sparse mixed products through chaotic mixing dynamics (e.g. Browne et al. , 2005;

581   Perugini and Poli, 2012; Morgavi et al., 2013; Fig. 15a-1). The petrologic characteristic of BP rock

582 (linear trend between WP, BP and BE in the 1/MgO vs FeO/MgO and in the Harker diagrams of both

583 glass and whole-rock compositions), the bimodal BP mineral assemblage (Fig. 4d) and the common

584 presence within BP of BE and WP inclusions (Figs. 2g; 4c), suggest that this pumice type likely

585 represent the product of the mixing between BE-forming magma and the rhyolitic host (Shaw, 2006;

586 Morgavi et al., 2013, 2018; Pritchard et al., 2013; Scruggs and Putirka, 2018). According to the applied

587 geothermometers (Fig. 14), during mafic recharge temperature of the host and injecting magma were

588 both high (respectively > 875 °C and ~ 1000 °C; see discussion Section 5.2; e.g. Ridolfi et al., 2016),

589 and thus, regardless the compositional differences (Fig. 8), the two magmatic endmembers could

590 locally mix and generate hybrid melts (e.g. Perugini and Poli; Plail et al., 2014; Fig. 15a). It is also

591 possible that mixing continued to some extent after quenching of BE magma, by a combination of

592 mechanical processes like disaggregation and dispersion of the enclave crystals and glass (Wiebe,

593 1996; Clynne, 1999; Streck and Grunder, 1999; Morgavi et al., 2013; 2016; Michel et al., 2017; Gogoi

594 and Saikia, 2018), as suggested by the presence of partially-dismembered BE material (quenched blobs

595 and phenocrysts) within WP and BP samples (Figs. 2c, g; 4c-f).

596 The oscillatory zoning of WP plagioclase, in which areas of variable anorthite contents alternate (Fig.

597 3c, d; Fig. 9a-b), can be associated to heating events affecting the melt in which plagioclase grows

598 (Tsuchiyama and Takahashi, 1983; Andrews et al., 2008; Shcherbakov et al., 2011), and also to

599 variable magmatic H_2O content, oxygen fugacity and pressure conditions (Housh and Luhr, 1991;

600 Coombs et al., 2000; Putirka, 2005). Considering the lack of evident resorption surfaces in WP

601 plagioclase (like those observed in BE plagioclase; Fig. 5i; e.g. Streck, 2008), and that the unique

602 equilibrium plagioclase-liquid pairs are those formed by the high anorthite zones of oscillatory grains

603 (Fig. 13) we interpret that oscillation in WP plagioclase was generated by variable conditions in the

604 magma (i.e. convective environment; e.g. Ginibre et al., 2002; Fig. 15b) likely due to the mafic

605 recharge event, and that the plagioclase grains that suffered resorption and re-crystallization are mainly

606 those transferred from the silicic host (WP) to BE-forming magma (Figs. 5i; 15b-2).

607 Leonard et al. (2002) proposed that enclave groundmass textures similar to BE can be generated by

608 undercooling crystallization after mafic magma receives H_2O by mixing with the rhyolitic host. Thus,

609 the generation of BE amphibole groundmass microlites (Fig. 6a-c) and corona-forming microlites (Fig.

610 6e, f) could be a consequence of both the mixing event and quenching. In this case, the variability in

611 Mg# between these amphibole crystals (Fig. 12c) would be due to different crystallization mechanisms

612 (i.e. crystallization from BE melt and from BE mafic phenocrysts, respectively). Moreover, BE

613 groundmass texture is not dyktitaxitic (e.g. Bacon, 1986; Mortazavi and Sparks, 2004; Browne et al.,

614 2005) because amphibole microlites are more tabular than acicular and do not form a continuous

615 crystal touching framework with plagioclase laths (Fig. 6b, c). Experimental works demonstrated that

616 for a dyktitaxitic texture to form, temperature contrast between the injecting and host magmas must be

617 $\geq$ 150 °C (Logfren, 1980; Coombs et al., 2003; Browne et al., 2005). Taking into account the relatively

618 high temperature calculated for WP and BE (Fig. 14a, b; Table 9A1-3), it is likely that the thermal

619 contrast between these two magmas was not high (lower than 150 °C; see discussion paragraph 6.2),

620 allowing for an initial stage of partial-liquid interaction between BE and WP magmas, which favored

621 magma mixing.

622 According to our reconstruction, FBE and CBE types represent a later mafic recharge event.

623 Differently from BE, the association of FBE/CBE is only present within the eruptive CPPI Phase II

624 deposits (Fig. 2f), and their reciprocal petrologic affinity (Figs. 8; 9d; 11; 12a, b) suggests that these

625 two enclave types are genetically related to the same parental magma (Fig. 15 b). The textural

626 differences between BE crystalline groundmass and FBE (Figs. 5b, c; 6a, b) indicate that FBE-forming

627 magma crystallized with a lower undercooling degree than BE (Shea and Hammer, 2013), which

628 corroborate the idea that FBE/CBE melt entered the rhyolitic chamber after BE magmatic injection.

629 The slight differences existing between FBE and CBE glass and mineral compositions (Figs. 8; 11; 12)

630 and mineral modal contents (Table 1) can be related to partial mixing with the silicic host (maybe BP-

631 melt), given the resorbed orthopyroxene cores within CBE crystal-rich inclusions (Figs. 7f) and the

632 similarity in the compositions of FBE and BP glass (Fig. 8c, d, g, h). However, this scenario contrast

633 with the geochemical whole rock (and glass) diagrams in which a linear trend between FBE/CBE and

634 BP sample is not evident (Fig. 8d, i). This suggests that the compositional differences between FBE

635 and CBE (Fig. 8a-h) may due, for example, to compositional heterogeneities in the FBE- and CBE-

636 forming magma, and not by a variable degree of chemical interaction with the host. However, the most

637 evident difference between FBE and CBE regards the crystalline texture (different crystal size and

638 contents; Figs. 6, 7), which indicate variable crystallization conditions (i.e. undercooling) at which this

639 magma crystallized (e.g. Conte et al., 2006; Shea and Hammer, 2013). Thus, it is possible that the

640 external part of the magmatic intrusion (FBE), at the interface with the silicic host where T contrast

641 was higher, crystallized a sub-millimetric (and equigranular) crystal assemblage (Fig. 6a; Fig. 15c-1, c-

642 2), while in the internal part of the intrusion (CBE), where T contrast was lower than the interface, the

643 magma crystallized a coarser mineral association (e.g. Browne et al., 2005; Fig. 15c-3, c4). The

644 presence within CBE of the crystal-rich inclusions (Figs. 2h; 7f) is in accord with the hypothesis that

645 crystallization (and crystal accumulation) did actually occurred (Fig. 15c-5). The amphibole barometric

646 results obtained from FBE and CBE indicate that crystallization may have started in an earlier pre-

647 injection magmatic stage (i.e. polybaric crystallization; Ridolfi et al., 2008). However, care must be

648 taken we interpreting the results of the Ridolfi and Renzulli, (2012) amphibole thermobarometer,

649 considering that the inferred undercooling conditions (i.e. disequilibrium) of crystallization (especially

650 for FBE and BE) are not suitable for this thermobarometric estimation (Ridolfi et al., 2010). More

651 considerations about this point will be discussed in section 6.2. Finally, during the eruption, distinct

652   parts of the reservoir were evacuated (Fig. 15c), with the first extraction of the upper rhyolitic magma

653   (higher SiO_2 WP) containing low abundance of BE and BP material (CPPI Phase I), and a second

654   event, which causes the withdraw of the deepest part of the reservoir (CPPI Phase II with WP, BP and

655   all the enclave types; Fig. 15c).

a) Injection of BE magma and chaotic interaction with WP host

$T_{WP} \sim 920 \ °C$

$T_{BE} \sim 1000 \ °C$ $T_{BP} \sim 960 \ °C$

Phase I WP Phase II WP
BP BE

0.5 mm

b) Injection of FBE/CBE magma

$T_{FBE/CBE \ magma} \sim 960 \ °C$

FBE/CBE magma injection FBE CBE

c) Pre-eruptive differential crystallization of FBE and CBE magma

1 mm

1 mm

$T_{(amp-rim)FBE} \sim 930 \ °C$ $T_{(amp)CBE} \sim 1000 \ °C$

BP CBE FBE

FBE CBE BP

1 cm
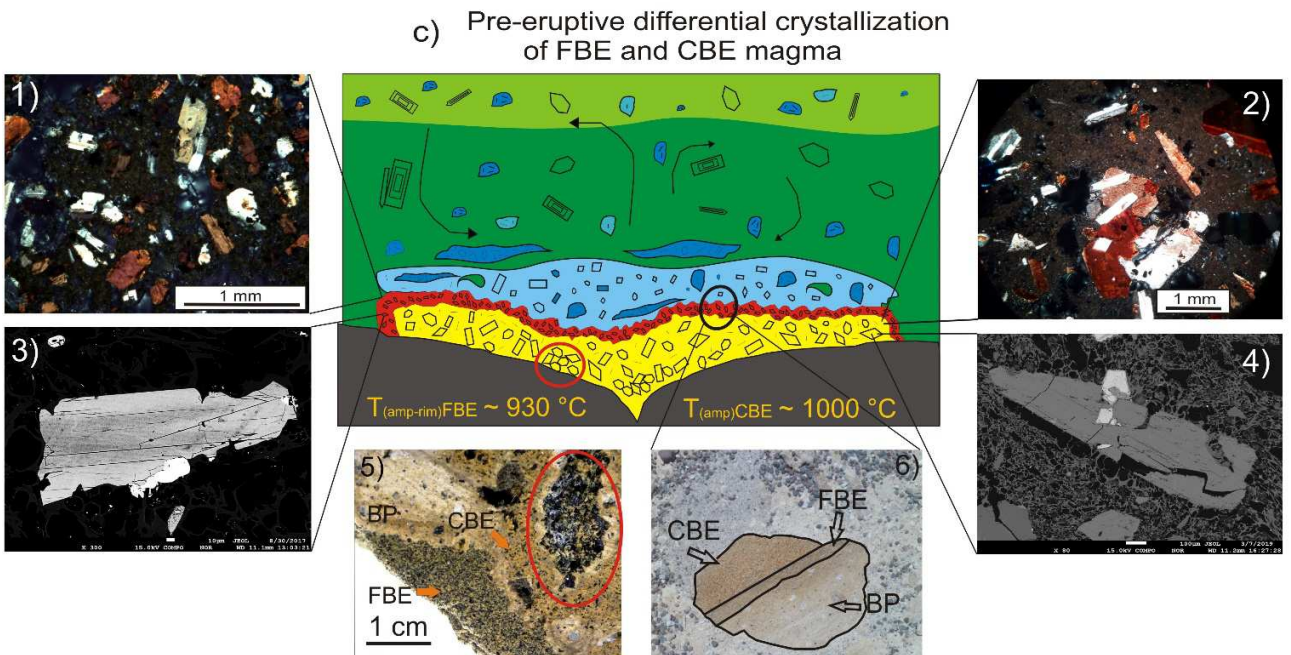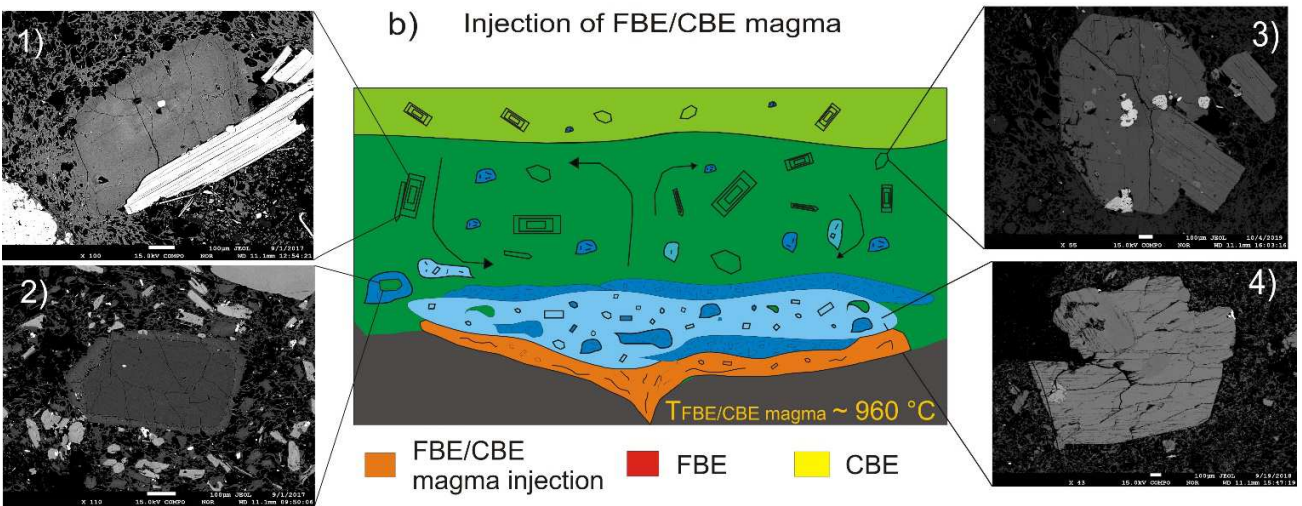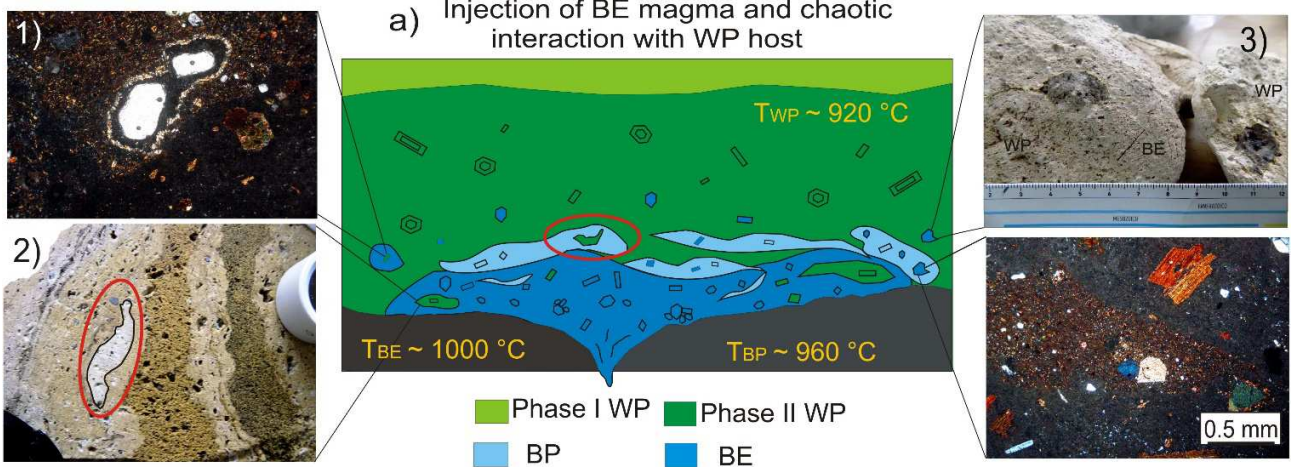
657　Figure 15. Simplified model of the pre-eruptive magmatic phases of the CPPI sub-volcanic system. a) Injection of BE
658　partial-liquid magma, with consequent engulfment of WP phenocrysts and glass (a1, Fig. 6j), formation of the hybrid
659　trachy-dacite (a2, Fig. 5d) with remnants of WP melt within the hybrid (a3, Fig 2g), and dispersion of BE blobs within WP
660　and BP (a4, Fig. 2e) b) Crystallization of BE groundmass and formation of amphibole rim on BE phenocrysts (b1, Fig. 6a)
661　and crystallization in the hybrid BP melt (b2, Fig. 6g). c) Injection of FBE/CBE-forming magma at liquid state. d)
662　Differential crystallization of FBE/CBE magma with higher cooling rates at the interface with the host (c1, Fig. 7a; d3, Fig.
663　7c) and lower cooling rates in the mafic intrusion interior (c2, Fig. 8a-b), with consequent formation of the crystal-rich
664　inclusions (c5, Fig. 2h); c6) banded pumice (Fig. 2c) in which CBE, FBE and the hybrid BP are in contact each other. The
665　relative volume of mafic magmas is exaggerated for clarity.

666　*6.2. Thermobarometric constraints*

667　The estimations of the intensive parameters obtained by the thermobarometric calculations add physical

668　constraints on the model discussed in section 6.1 (Fig. 15), which is principally based on the petrologic

669　and textural characteristics of the silicic pumice and enclaves. The application of the distinct methods

670　provided a wide range of crystallization conditions, from middle to shallow crustal levels (~9 – 0 Kbar)

671　and between ~1180 – 800 °C (Fig. 14), reflecting the heterogeneity of the mineral assemblages and

672　textures in the CPPI products. We discussed in section 6.1 that mixing between BE- and WP-forming

673　magma was favored by the relatively high temperature of the rhyolitic host, and that the lack of a

674　dyktitaxitic texture on BE groundmass indicates a thermal contrast < 150 °C between the rhyolitic and

675　mafic magmas. Thermometric results confirm this reconstruction, showing that the average value of the

676　two-feldspars geothermometer (T = 890 °C) is within 150 °C respect the two-pyroxenes, amphibole,

677　and plagioclae-liquid calculated temperatures for BE, FBE and CBE (950 – 1000 °C; Fig. 14). Also the

678　plagioclase-liquid and clinopyroxene-liquid methods, which provided a higher temperature range

679　(~900-950) than the former one, are in accord with this assumption (Fig. 14). Considering the average

680　clinopyroxene-liquid temperature calculated for WP (~ 900 °C,) as that of the rhyolitic host at the time

681　of mafic recharge, and the two-pyroxenes temperature of BE (990 ° C) as the temperature of the

682　injecting magma, the thermal contrast between WP- and BE-forming magmas would be lower than 100

683　°C (ca. 90 °C).

684 Among the enclave types, BE display the more heterogeneous crystal cargo, carrying a pre-injective

685 mafic crystalline association (Figs. 5a, d, e, l), a post-injection quenched crystal groundmass (Fig. 5b,

686 c), and a minor xenocrystic component derived from the mingling with the rhyolitic host (Figs. 5i, j, k;

687 15a). This complexity is reflected in the variability of BE T-P results, with the orthopyroxene-liquid,

688 the clinopyroxene-liquid and the olivine-liquid thermobarometric models that yielded the highest

689 temperatures (~1100 - 1175 °C; Fig. 14) and high pressures ranges (~6.0 – 8.8 Kbar; Fig. 14). These

690 conditions may represent the deep stagnation level where BE magma crystallized and cooled (e.g.

691 Ridolfi et al., 2016; Lucci et al., 2020). The presence of clinopyroxene and orthopyroxene crystal

692 aggregates (Figs. 5d; 8A-6) is in accord with this assumption, and the two-pyroxene calculated

693 temperature range (~ 950-1000 °C, average 992 ± 6 °C) indicates that cooling and crystallization of BE

694 magma proceeded up to ca. 1000 °C (Fig. 14). BE amphibole phenocrysts (Fig. 5l) may be related to

695 this lower-T magmatic stage (~ 950 – 990 °C) at deep levels in the crust (P = 7.4 – 9.0 Kbar), prior to

696 the ascent of BE magma toward the surface.

697 The two direct barometric estimates of WP samples yielded comparable results (Fig. 14), and indicate a

698 shallow crustal depth at about 2.6-2.7 Kbar, similarly to the pressure calculated using the BE

699 clinopyroxene – orthopyroxene pairs (P = 3.0 ± 0.35 Kbar). The plagioclase-liquid pressure estimations

700 for FBE and CBE results are more variable, with average values of 3.4 ± 0.6 Kbar and 1.8 ± 0.4 Kbar,

701 respectively. On the basis of these calculations, we infer that the crustal level at which the silicic and

702 mafic magmas interacted lays at a depth of ca. 10 Km (estimated considering an upper crustal density

703 of 2.74 Kg dm^{-3}; e.g. Lucci et al., 2020), a position that can be considered the deepest portion of the

704 CPPI reservoir (e.g. Ridolfi et al., 2008). The FBE and CBE pressure estimates indicate a wide

705 crystallization pressure range (1.0 – 7.8 Kbar; Fig. 14) and the estimation of the depth of this reservoir

706 before the magmatic ascent remains uncertain. We assumed the textural characteristic of FBE and CBE

707 amphiboles (differently from BE amphibole groundmass microlites) as suitable for the Ridolfi and

708   Renzulli, (2012) model, although the undercooling conditions inferred for FBE and CBE amphiboles

709   (Fig. 15c-1, c2), and the T-P distribution of CBE amphibole core-rim analyses (Fig. 14), suggest the

710   occurrence of disequilibrium crystallization during amphibole growth (Ridolfi et al., 2010; Gorini et

711   al., 2018). By consequence, the amphibole thermobarometer of Ridolfi and Renzulli, (2012) would not

712   be applicable to our rocks, and the pressure results of CBE and FBE amphibole may be overestimated

713   (Ridolfi and Renzulli 2012; Gorini et al., 2018). However, it is interesting to note that the rims of FBE

714   amphiboles, which should have crystallized with higher temperature contrast than those within CBE,

715   provide temperature and pressure ranges (914 – 940 °C, and 2.5 – 3.3 Kbar) comparable with the T-P

716   results obtained from WP phenocrysts (clinopyroxene- and plagioclase-liquid methods; Fig. 14), which

717   likely reflect the physical conditions of the rhyolitic reservoir. This thermobarometric convergence

718   (Fig. 14) and the homogeneous composition of FBE amphibole rims (Fig. 12a, b) suggest that a

719   chemical re-equilibration of these amphibole crystals may have occurred (e.g. Ridolfi et al., 2016;

720   Gorini et al., 2018; Fig. 14). Thus, the amphibole T-P estimates of Ridolfi and Renzulli (2012) may be

721   valid in those cases where amphibole crystallized under disequilibrium and then re-equilibrated with

722   the physical conditions of the host reservoir.

723   The occurrence of the re-equilibration event implies that an interval of time must have passed between

724   amphibole crystallization and the starting of the Plinian eruption. Chemical zoning on BE and CBE

725   amphibole was not detected, and this contrasts with the hypothesis of re-equilibration, although a

726   slight T-P differentiation is present in BP core-rim phenocrysts (Figs. 14). Possibly, BE amphiboles

727   (groundmass and phenocrysts) were protected from the surrounding magmatic environment by the

728   quenched glassy material, or zoning was not detected during EPMA study. CBE amphiboles, as

729   discussed previously (Fig. 15c), were preserved in the deeper (and hotter) part of the reservoir and did

730   not have the sufficient time (and/or thermal contrast) to re-equilibrate. The occurrence of the proposed

731   temporal gap is also consistent with the thermometric results obtained from the Zr-saturation model (~

732   790 ± 15 °C), which is indicative of the pre-eruptive magmatic thermal state (e.g. Lucci et al., 2018)

733   and suggest the occurrence of a cooling stage to about 800 °C before the beginning of the eruption

734   (Fig. 14).

735   These textural and thermometric evidences are in accordance with the existence of a temporal interval

736   between the FBE/CBE magmatic injection/crystallization and the eruption, and contrast with the

737   hypothesis of a strong temporal coincidence between mafic recharge and the volcanic event (e.g.

738   Leonard et al., 2002). According to this reconstruction, the rhyolitic eruption likely occurred during a

739   cooling stage rather than a thermal peak, indicating that other possible factors (like the tectonic control)

740   may have played an important role as an eruption trigger (as already suggested by Báez et al., 2015).

741   The low volume abundance of the mafic products in the CPPI deposits sustains this idea,

742   strenghthening the hypothesis that the thermal and chemical consequences of the mafic recharge,

743   although increasing the pressure in the reservoir by volatile exsolution (e.g. Folch and Marti, 1998),

744   were not the main factor in triggering the Campo de la Piedra Pómez eruption.

745   **6. Conclusions**

746   The study of the petrologic characteristics of the CPPI indicates the presence in the ignimbritic deposits

747   of different juvenile clasts (silicic pumice and magmatic enclaves), which record the complex pre-

748   eruptive history of magmatic interactions (physical and chemical), during which magmas developed

749   diffuse macro- and micro-mingling textures. The main conclusions obtained in this work are the

750   following: (i) BE-forming magma is one that most interacted with the rhyolitic host, both physically

751   (diffuse and complex micro-mingling textures) and chemically (hybridization with the rhyolite to form

752   trachydacitic pumice), (ii) mixing between BE and WP started during the initial stage of BE mafic

753   recharge and was favored by the relative high temperature of the rhyolitic host (≥ 875 °C, temperature

754   contrast of ca. 90 °C) calculated with distinct geothermometers, (iii) FBE and CBE reflect a second

755 magmatic injection event, and their textural variability is related to different degree of undercooling.

756 FBE crystallized at the interface with the more silicic magma, while CBE reflects crystallization in a

757 deeper and hotter zone of the Campo de la Piedra Pómez reservoir, (iv) the convergence of different

758 barometric methods (using the rhyolite and enclaves compositions) indicates that the interaction among

759 rhyolitic and mafic magmas occurred at a depth of 2.6-2.7 Kbar (~ 10 Km b.s.l.), a level which can be

760 considered as the basal portion of the Campo de la Piedra Pómez magmatic system. Finally, we

761 conclude that a temporal gap existed between the last event of mafic recharge/crystallization and the

762 eruption, during which FBE amphibole had the time to re-equilibrate with the reservoir conditions and

763 the rhyolitic magma cooled down to the temperature of eruption (~ 800 °C).

772 *References*

773 Abdel-Rahman, A. F. M. (1994). Nature of biotites from alkaline, calc-alkaline, and peraluminous

774   magmas. Journal of petrology, 35(2), 525-541. https://doi.org/10.1093/petrology/35.2.525.

775 Aceñolaza, F.G., Toselli, A.J., González, O., (1976). Geología de la región comprendida entre el salar

776   del Hombre Muerto y Antofagasta de la Sierra, provincia de Catamarca. Rev. Asoc. Geol.

777   Argent. 31 (2), 127–136.

778   Allmendinger, R.W., Strecker, M., Eremchuk, J:E., Francis, P., (1989). Neotectonic deformation of
779   the southern Puna Plateau, northwestern Argentina. Journal of South American Earth
780   Sciences, 2, 111-130. https://doi.org/10.1016/0895-9811(89)90040-0.

781   Andrews, B.J., Gardner, J.E., Housh, T.B., (2008). Repeated recharge, assimilation, and hybridization
782   in magmas erupted from El Chichón as recorded by plagioclase and amphibole phenocrysts.
783   Jounral   of   Volcanology   and   Geothermal   Research,   175,   415-426.
784   https://doi.org/10.1016/j.jvolgeores.2008.02.017.

785   Arnosio, M., Becchio, R., Viramonte, J.G., Groppelli, G, Norini G. and Corazzato, C., (2005).
786   Geología del Complejo Volcánico Cerro Blanco (26° 45` LS- 67° 45` LO), Puna Austral.
787   Actas 16º Congreso Geológico Argentino 1: 851-858. La Plata.

788   Arnosio, M., (2010). Evidencia textural y geoquímica de mezcla de magmas en el Volcán Chimpa,
789   Puna Salteña. Revista de la Asociación Geológica Argentina 66 (1), 253-270.

790   Bacon, C. R., (1986). Magmatic inclusions in silicic and intermediate volcanic rocks. Journal of
791   Geophysical Research 91 (B6): 6091-6112. https://doi.org/10.1007/BF01150292.

792   Bacon, C. R., (2011). Magmatic enclaves. American Geophysical Union, Fall Meeting 2011, abstract
793   id. V41F-01.

794   Báez, W., Arnosio, M., Chiodi, A., Ortiz-Yañes, A., Viramonte, J. G., Bustos, E., Giordano, G.,
795   López, J. F., (2015). Estratigrafía y evolución del Complejo Volcánico Cerro Blanco, Puna
796   Austral, Argentina. Revista Mexicana de Ciencias Geológicas 32 (1): 29-49.

797   Báez, W., Chiodi, A., Bustos, E., Arnosio, M., Viramonte, J. G., Giordano, G., Alfaro Ortega, B.,
798   (2017a). Mecanismos de emplazamiento y destrucción de los domos lávicos asociados a la
799   caldera Cerro Blanco, Puna Austral. Revista Geologica Argentina, vol 74 (2), pp. 223-238.

800   Báez, W., Nuñez, G. C., Giordano, G., Viramonte, J. G., and Chiodi, A. (2017b). Polycyclic scoria

801   cones of the Antofagasta de la Sierra basin, Southern Puna plateau, Argentina. Geological

802   Society, London, Special Publications, 446(1), 311-336.

803   Báez, W., de Silva, S., Chiodi, A, Bustos, E., Giordano G., Arnosio, M., Suzaño N., Viramonte, J.G.,

804   Norini, G. and Groppelli, G. (2020a). Pulsating flow dynamics of sustained, forced Pyroclastic

805   Density Currents: Insights from a facies analysis of the Campo de la Piedra Pómez Ignimbrite,

806   southern Puna, Argentina. Bulletin of volcanology (in press).

807   Báez, W., Bustos, E., Chiodi, A., Reckziegel, F., Arnosio, M., de Silva, S., Viramonte J.G. Sampietro

808   M.M. and Peña-Monné, J. L. (2020b). Eruptive style and flow dynamics of the pyroclastic

809   density currents related to the Holocene Cerro Blanco eruption (Southern Puna plateau,

810   Argentina). Journal of South American Earth Sciences, 98, 102482.

811   Baranzangi, M., Isacks, B.L., (1976). Spatial distribution of earthquakes and subduction of the Nazca

812   plate beneath South America. Geology 4 (11), 686-692. https://doi.org/10.1130/0091-

813   7613(1976)4<686:SDOEAS>2.0.CO;2.

814   Bianchi, M., Heit, B., Jakolev, A., Yuan, X., Kay, S.M., Sandvol, E., Alonso, R.N., Coira, B., Brown,

815   L., Kind, R., Comte, D., 2013. Teleseismic tomography of the southern Puna plateau in

816   Argentina   and   adjacent   regions.   Tectonophysics   586,   65-83.

817   https://doi.org/10.1016/j.tecto.2012.11.016.

818   Blake, S., Fink, J.H., (2000). On the deformation and freezing of enclaves during magma mixing.

819   Journal of Volcanology and Geothermal Research 95, 1-8. https://doi.org/10.1016/S0377-

820   0273(99)00129-8.

821   Browne, B.L:, Eichelberger,J.C., Patino, L.C., Vogel, T.A., Dehn, J., Uto, K., Hoshizumi, H.,

822   (2005). Generation of porphyritic and equigranular mafic enclaves during magma recharge

823   events at Unzen volcano, Japan. Journal of Petrology, 47 (2), 301-328.

824   https://doi.org/10.1093/petrology/egi076.

825   Bustos, E., Báez, W., Norini, G., Arnosio, M., de Silva, S.L., (2018). The geological and structural

826   evolution of the long-lived Miocene-Pleistocene La Hoyada Volcanic Complex in the

827   geodynamic framework of the Central Andes, Argentina. Journal of Volcanology and

828   Geothermal Research. https://doi.org/10.1016/j.jvolgeores.2018.07.010.

829   Calzolari, G., Rossetti, F., Ault, A.K., Olivetti, V., Nozaem, R., (2018). Hematite (U-Th)/He

830   thermocronometry constrains intraplate strike-slip faulting on the Kuh-e-Faghan Fault,

831   central Iran. Tectonophysics 728, 41-54.

832   Clarke, .B., (1981). The mineralogy of peraluminous granites: a review. The Canadian Mineralogist

833   19, 3-17.

834   Clynne, M. A., (1999). A complex magma mixing origin for rocks erupted in 1915, Lassen Peak,

835   California. Journal of Petrology 40 (1): 105-132. https://doi.org/10.1093/petroj/40.1.105.

836   Coombs, M.C., Eichelberger, J.C., Rutherford, M.J., (2000). Magma storage and mixing conditions

837   for the 1953-1974 eruptions of Southwest Trident volcano, Katmai National Park, Alaska.

838   Contribution to Mineralogy and Petrology 140, 99-118.

839   https://doi.org/10.1007/s004100000166.

840   Coombs, M.C., Eichelberger, J.C., Rutherford, M.J., (2003). Experimental and textural constraints

841   on mafic enclave formation in volcanic rocks. Journal of Volcanology and Geothermal

842   Research 119, 125-144. https://doi.org/10.1016/S0377-0273(02)00309-8.

843   Coombs, M., Gardner, J. E., (2004). Reaction rim growth on olivine in silicic melt: Implications for

844   magma mixing. American Mineralogist 89: 748-759. https://doi.org/10.2138/am-2004-5-608.

845   Couch, S., Sparks, R.S.J., Carrol, M.R., (2001). Mineral disequilibrium in lavas explained by
846   convective self-mixing in open magma chambers. Nature, 441, 1037-1039.

847   De Hoog, J.C.M., Hattori, K.H., Hoblitt, R.P., (2004). Oxidized sulfur-rich mafic magma at Mount
848   Pinatubo, Philippines. Contribution to mineralogy and Petrology 146, 750-761.
849   https://doi.org/10.1007/s00410-003-0532-4.

850   De Silva, S. L., (1989). Altiplano-Puna Volcanic Complex of Central Andes. Geology 17, 1102-
851   1106. https://doi.org/10.1130/0091-7613(1989)017<1102:APVCOT>2.3.CO;2.

852   De Silva, S.L., Gosnold, W.D., (2007). Episodic construction of batholith: insights from the
853   spatiotemporal development of an ignimbrite flare-up. Journal of Volcanology and
854   Geothermal Research 167, 320-355. https://doi.org/10.1016/j.jvolgeores.2007.07.015.

855   Eichelberger, J.C., (1980). Vesiculation of mafic magma during replenishment of silicic magma
856   reservoirs. Nature, 288, 446-450. https://doi.org/10.1038/288446a0.

857   Fernández Seveso, F., M. Perez, I. Brisson, I. and Alvarez, L. (1991). Análisis estratigráfico
858   secuencial de la cuenca de Paganzo. Depósitos marinos y continentales del Paleozoico
859   superior en el oeste argentino. Informe interno YPF. Mendoza (Unpublished).

860   Filipovich, R., Báez, W., Bustos, E., Villagrán, A., Chiodi, A., Viramonte, J.G., (2019). Estilos
861   eruptivos asociados al volcanismo monogenético máfico de la región de Pasto Ventura, Puna
862   Austral, Argentina. Andean Geology 46 (2), 300-335. https://doi.org/10.5027/andgeoV46n2-
863   3091.

864   Folch, A., Marti, J., (1998). The generation of overpressure in felsic magma chambers by
865   replenishment. Earth and Planetary Science Letters 163, 301-314.
866   https://doi.org/10.1016/S0012-821X(98)00196-4.

867   Ginibre, C., Kronz, A., Wörner, G., (2002). High-resolution quantitative imaging of plagioclase

868   composition using accumulated backscattered electron images: new constraints on oscillatory

869   zoning. Contribution to Mineralogy and Petrology 142, 436-448.

870   https://doi.org/10.1007/s004100100298.

871   Gogoi, B., Saikia, A., (2018). The role of viscous folding in magma mixing. Chemical Geology 501,

872   26-34. https://doi.org/10.1016/j.chemgeo.2018.09.035.

873   Gorini, A., Ridolfi, F., Piscaglia, F., Taussi, M., Renzulli, A., (2018). Application and reliability of

874   calcic amphibole thermobarometry as inferred from calc-alkaline products of active

875   geothermal areas in the Andes. Journal of Volcanology and Geothermal Research 358, 58-

876   76. 10.1016/j.jvolgeores.2018.03.018.

877   Guzmán, S., Grosse, P., Montero-López, C., Hongn, F., Pilger, R., Petrinovic, I & Aramayo, A.

878   (2014). Spatial–temporal distribution of explosive volcanism in the 25–28 S segment of the

879   Andean Central Volcanic Zone. Tectonophysics, 636, 170-189.

880   https://doi.org/10.1016/j.tecto.2014.08.013.

881   Haag, M.B., Baez, W.A., Sommer, C.A., Arnosio, J.M., Filipovich, R.E., (2019). Geomorphology

882   and spatial distribution of monogenetic volcanoes in the southern Puna Plateau (NW

883   Argentina). Geomorphology 342, 296-209. https://doi.org/10.1016/j.geomorph.2019.06.008.

884   Heit, B., Bianchi, M., Yuan, X., Kay, S.M., Sandvol, E., Kumar, P., Kind, R., Alonso, R.N., Brown,

885   L.D., Comte, D., (2014). Structure of the crust and the lithosphere beneath the southern Puna

886   plateau from teleseismic receiver functions. Earth and Planetary Science Letters 385, 1-11.

887   https://doi.org/10.1016/j.epsl.2013.10.017.

888 Heiken, G., Eichelberger, J.C., (1980). Eruptions at Chaos Crags, Lassen Volcanic National Park,

889   California. Journal of Volcanology and Geothermal Research, 7, 443-481.

890   https://doi.org/10.1016/0377-0273(80)90042-6.

891 Hernando, I.R., Petrinovic, I.A., LLambías, E.J., D'Elia, L., Gonzáles, P.D., Aragón, E., (2016). The

892   role of magma mixing and mafic recharge in the evolution of a back-arc quaternary caldera:

893   The case of Payún Matrú. Journal of Volcanology and Geothermal Research, 311, 150-169.

894   https://doi.org/10.1016/j.jvolgeores.2016.01.008.

895 Housh, T.B., Luhr, J.F., (1991). Plagioclase-melt equilibria in hydrous systems. American

896   Mineralogist 76 (3-4), 477-492.

897 Humphreys, M., Christopher, T., Hards, V., (2009). Microlite transfer by disaggregation of mafic

898   inclusions following magma mixing at Soufrière Hills volcano, Montserrat. Contribution to

899   Mineralogy and Petrology 157, 609-624. https://doi.org/10.1007/s00410-008-0356-3.

900 Huppert, H.E., Sparks, R.S.J., Turner, J.S., (1982). Effects of volatiles on mixing in calc-alkaline

901   magma systems. Nature 297, 554-557. https://doi.org/10.1038/297554a0.

902 James, D. E. (1971). Plate tectonic model for the evolution of the Central Andes. Geological Society

903   of America Bulletin, 82(12), 3325-3346. https://doi.org/10.1130/0016-

904   7606(1971)82[3325:PTMFTE]2.0.CO;2.

905 Jordan, T.E., Isacks, B.L., Ramos, V.A., Allmendinger, R.W., (1983). Mountain buildings in the

906   Central Andes. Episodes, 3, 20-26. https://doi.org/10.1029/JB094iB04p03891.

907 Kay, S. M., Coira, B., and Viramonte, J., (1994). Young mafic back arc volcanic rocks as indicators

908   of continental lithospheric delamination beneath the Argentine Puna Plateau, central Andes:

909   Journal of Geophysical Research, v. 99, p. 24,323-24,339. 24323-24339.

910   https://doi.org/10.1029/94JB00896.

911   Kay, S.M., Coira, B., Mpodozis, C., (2006). Late Neogene volcanism in the Cerro Blanco region of

912   the Puna Austral, Argentina (~26.5°S, ~67.5°W). XI Congreso Geológico Chileno 7-11

913   august 2006. Actas vol. 2 Volcanismo y magmatismo.

914   Kay S.M., Coira, B.L., Caffe, P.J., Chen, C-H., (2010). Regional chemical diversity, cristal and

915   mantle sources and evolution of central Andean Puna Plateau Ignimbrites. Journal of

916   Volcanology   and   Geothermal   Research   198   (1-2),   81-111.   doi:

917   10.1016/j.jvolgeores.2010.08.013.

918   Koyaguchi, T., (1985). Magma mixing in a conduit. Journal of Volcanology and Geothermal

919   Research 25, 365-369. https://doi.org/10.1016/0377-0273(85)90022-8.

920   Le Bas, M. J., Le Maitre, R. W., Streckeisen, A., Zanettin, B., (1986). A chemical classification of

921   volcanic rocks based on total alkali-silica diagram. Journal of Petrology 27 (3): 745-750.

922   https://doi.org/10.1093/petrology/27.3.745.

923   Leonard, G. S., Cole, J. W., Nairn, I. A., Self, S., (2002). Basalt triggering of the c. AD 1305

924   Kaharoa rhyolite eruption, Tarawera Volcanic Complex, New Zealand. Journal of

925   Volcanology and Geothermal Research 115: 461-486. https://doi.org/10.1016/S0377-

926   0273(01)00326-2.

927   Locock, A. J., (2014). An Excel spreadsheet to classify chemical analyses of amphiboles following

928   the   IMA   2012   reccomendations.   Computers   and   Geosciences   62,   1-11.

929   https://doi.org/10.1016/j.cageo.2013.09.011.

930   Logfren, G.E., (1980). Experimental studies on the dynamic crystallization of silicate melts. In

931   Hargraves, R.B., (ed.) Physics of magmatic processes. Princeton, NJ: Princeton University

932   Press, 487-551.

933   Lucci, F., Rossetti, F., Becchio, R., Theye, T., Gerdes, A., Optiz, J., Báez, W., Bardelli, L., De Astis,

934   G., Viramonte, J., Giordano, G., (2018). Magmatic Mn-rich garnets in volcanic arc settings:

935   Age and longevity of the magmatic plumbing system of the Miocene Ramadas volcanism

936   (NW Argentina). Lithos 322, 238-249. https://doi.org/10.1016/j.lithos.2018.10.016.

937   Lucci, F., Carrasco-Nuñez, G., Rossetti, F., Theye, T., White, J.C., Urbani, S., Azizi, H., Asahara,

938   Y., Giordano, G., (2020). Anatomy of the plumbing system of Los Humeros Caldera

939   (Mexico): implication for geothermal systems. Solid Earth 11, 125-159. 125-159.

940   DOI:10.5194/se-11-125-2020.

941   Maro, G., and Caffe, P. J. (2017a). Neogene monogenetic volcanism from the Northern Puna region:

942   products and eruptive styles. Geological Society, London, Special Publications, 446(1), 337-

943   359.Maro, G., Caffe, P. J., Romer, R. L., Trumbull, R. B. (2017b). Neogene mafic

944   magmatism in the northern Puna Plateau, Argentina: Generation and evolution of a back-arc

945   volcanic suite. Journal of Petrology, 58(8), 1591-1617.

946   Maro, G., Caffe, P. J., y Báez, W. (2017c). Volcanismo monogenético máfico cenozoico de la Puna.

947   In Ciencias de la Tierra y Recursos Naturales del NOA. Relatorio del XX Congreso

948   Geológico Argentino, San Miguel de Tucumán (Vol. 2017). Asociación Geológica

949   Argentina.

950   Maro, G., (2019). Estudio de magmas máficos de la Puna Argentina: Variaciones en la evolución

951   magmática relacionadas al transporte de Cu. XIII congreso de Mineralogía, Petrología ígnea

952   y metamórfica, y Metalogénesis, 7-9 august, Córdoba, Acta, 134-135.

953   Martin, V.M., Pyle, D.M., Holness, M.B., (2006). The role of crystal framework in the preservation

954   of enclaves during magma mixing. Earth and Planetary Science Letters, 248, 787-799.

955   https://doi.org/10.1016/j.epsl.2006.06.030.

956   Michel, L., Wenzel, T., Markl, G., (2017). Interaction between two contrasting magmas in the Albtal

957   pluton (Schwarzwald, SW Germany): textural and mineral-chemical evidence. International

958   Journal of Earth Science 106 (5), 1505-1524. 1505-1524. https://doi.org/10.1007/s00531-

959   016-1363-7.

960   Miller, C.F., McDowell, S.M., Mapes, R.W:, (2003). Hot and cold granites? Implications of zircon

961   saturation temperatures and preservation of inheritance. Geology 31 (6), 529-532.

962   https://doi.org/10.1130/0091-7613(2003)031<0529:HACGIO>2.0.CO;2.

963   Montero-López, M. C., Hongn, F., Brod, J. A., Seggiaro, R., Marrett R. y Sudo, M., (2010).

964   Magmatismo ácido del Mioceno Superior-Cuaternario en el área de Cerro Blanco-La

965   Hoyada, Puna Sur. Revista de la Asociación Geológica Argentina, 67 (3): 329-348.

966   Morgavi, D., Perugini, D., De Campos, C. P., Werner, E-I., Dingwell, D. B., (2013). Time evolution

967   of exchanges during mixing of rhyolite and basaltic melts. Contribution to Mineralogy and

968   Petrology 166: 615-638. https://doi.org/10.1007/s00410-013-0894-1.

969   Morgavi, D., Arzilli, F., Pritchard, C., Perugini, D., Mancini, L., Larson, Dingwell, D.B., (2016).

970   The Grizzly Lake complex (Yellowstone Volcano, USA): Mixing between basalt and

971   rhyolite unrevealed by microanalysis and X-ray microtomography. Lithos 260, 457-474.

972   https://doi.org/10.1016/j.lithos.2016.03.026.

973   Morimoto, N. (1988). Nomenclature of pyroxenes. Mineralogy and Petrology 39, 55-76.

974   https://doi.org/10.1007/BF01226262.

975   Mortazavi, M., Sparks, R.S.J., (2004). Origin of rhyolite and rhyodacite lavas and associated mafic

976   inclusions of Cape Akrotiri, Santorini: the role of wet basalt in generating calcalkaline silicic

977   magmas.   Contribution   to   Mineralogy   and   Petrology,   146,   397-413.

978   https://doi.org/10.1007/s00410-003-0508-4.

979   Murphy, M.D., Sparks, R.S.J., Barclay, J., Carrol, M.R., Lejeune, A-M., Brewer, T.S., Macdonald,
980   R., Black, S., Young, S., (1998). The role of magma mixing in triggering the current eruption
981   at the Soufrière Hills volcano, Montserrat, West Indies. Geophysical Research Letters,
982   25(18), 3433-3436. https://doi.org/10.1029/98GL00713.

983   Murphy, M.D., Sparks, R.S:J., Barclay, J., Carrol, M.R., Brewer, T.S., (2000). Remobilization of
984   andesite magma by intrusion of mafic magma at the Soufriere Hills Volcano, Montserrat,
985   West Indies. Journal of Petrology, 41(19, 21-42. https://doi.org/10.1093/petrology/41.1.21.

986   Namur, O., Charlier, B., Toplis, M.J., Vander Auwera, J., (2012). Prediction of plagioclase-melt
987   equilibria in anhydrous silicate melts at 1 atm. Contributions to Mineralogy and Petrology
988   163, 133-150.

989   Pallister, J.S., Hoblit, R.P., Reyes, A., (1992). A basalt trigger for the 1991 eruptions of Pinatubo
990   volcano? Letters to Nature, 356, 426-428. https://doi.org/10.1038/356426a0.

991   Perugini, D., Poli, G., (2012). The mixing of magmas in plutonic and volcanic environments:
992   Analogies and differences. Lithos 153: 261-277. https://doi.org/10.1016/j.lithos.2012.02.002.

993   Plail, M. and Barclay, J. and Humphreys, M.C.S. and Edmonds, M. and Herd, R.A. and Christopher,
994   T.E., (2014). Characterization of mafic enclaves in the erupted products of Soufrière Hills
995   Volcano, Montserrat, 2009 to 2010. Memoirs, 39, 343-360. https://doi.org/10.1144/M39.18.

996   Plail, M., Edmonds, M., Woods, A.W., Barclay, J., Humphreys, M.C.S., Herd, R.A:, Christopher,
997   T., (2018). Mafic enclaves record syn-eruptive basalt intrusion and mixing. Earth and
998   Planetary Science Letters, 484, 30-40. https://doi.org/10.1016/j.epsl.2017.11.033.

999   Pritchard, C.J., Larson, P.B., Spell, T.L., Tarbert, K:D., (2013). Eruption-triggered mixing of extra-
1000   caldera basalt and rhyolite complexes along the East Gallatin-Washburn fault zone,

Yellowstone National Park, WY, USA. Lithos 175-176, 163-177. https://doi.org/10.1016/j.lithos.2013.04.022.

Putirka, K.A., (2005). Igneous thermometers and barometers based on plagioclase plus liquidus equilibria: tests of some existing models and new calibrations. American Mineralogist 90 (2-3), 336-346. https://doi.org/10.2138/am.2005.1449.

Putirka, K.A., Perfit, M., Ryerson, F.., Jackson, M.G., (2007). Ambient and excess mantle temperatures, olivine thermometry, and active vs. passive upwelling. Chemical Geology 241, 177-206. https://doi.org/10.1016/j.chemgeo.2007.01.014.

Putirka, K.D., Thermometers and barometers for volcanic systems, (2008). Reviews in Mineralogy & Geochemistry, 69, 61-120. https://doi.org/10.2138/rmg.2008.69.3.

Ridolfi, F., Puerini, M., Renzulli, A., Menna, M., Toulkeridis, T., (2008). The magmatic feeding system of El Reventador volcano (Sub-Andean zone, Ecuador) constrained by texture, mineralogy and thermobarometry of the 2002 erupted products. Journal of Volcanology and Geothermal Research, 176, 94-106. https://doi.org/10.1016/j.jvolgeores.2008.03.003.

Ridolfi, F., Renzulli, A. y Puerini, M., (2010). Stability and chemical equilibrium of amphibole in calc-alkaline magmas: an overview, new thermobarometric formulations and application to subduction-related volcanoes: Contributions to Mineralogy and Petrology 160: 45-66. https://doi.org/10.1007/s00410-009-0465-7.

Ridolfi, F., Renzulli, A. (2012). Calcic amphibole in calc-alkaline and alkaline magmas: thermobarometric and chemometric empirical equation valid up to 1,130 °C and 2.2 GPa. Contrib. Mineral. Petrol. (163), pp. 877-895. https://doi.org/10.1007/s00410-011-0704-6.

Ridolfi, F., Braga, R., Cesare, B., Renzulli, A., Perugini, D., Del Moro, S., (2016). Unravelling the complex interaction between mantle and crustal magmas encoded in the lavas of San

1024   Vincenzo (Tuscany, Italy). Part 1: Petrography and Thermobarometry. Lithos 244, 218-232.

1025   https://doi.org/10.1016/j.chemgeo.2007.01.014.

1026   Ridolfi, F., Zanetti, A., Renzulli, A., Perugini, D., Holtz, F., Oberti, R., (2018) AMFORM, a new

1027   mass-based model for the calculation of the unit formula of amphiboles from electron

1028   microprobe analyses. American Mineralogist 103, 1112-1125. https://doi.org/10.2138/am-

1029   2018-6385.

1030   Richards, J.P., Ullrich, T., Kerrich, R., (2006). The Late-Miocene Antofalla volcanic complex,

1031   southern Puna, NW Argentina: Protracted history, diverse petrology, and economic potential.

1032   Journal of Volcanology and Geothermal Research 152, 197-239.

1033   https://doi.org/10.1016/j.jvolgeores.2005.10.006.

1034   Risse, A., Trumbull, R.B., Kay, S.M., Coira, B., Romer, R.L., (2013). Multi-stage evolution of late

1035   Neogene mantle-derived magmas from the Central Andes back-arc in the southern Puna

1036   plateau of Argentina. Journal of Petrology 54, 1963-1995.

1037   Roberge, J., de Silva, S., Arnosio, M., Becchio, R., & Viramonte, J. G. (2008). Contrasting volatile

1038   contents in Central Andean ignimbrites of different volumes: implications for eruptive

1039   mechanisms (resumen), In International Association of Volcanologists and Chemical Earth's

1040   Interior General assembly, Reykjavík, Iceland: International Association of Volcanologists

1041   and Chemical Earth's Interior, 1.

1042   Ruprecht, P., Wörner, G., (2007). Variable regimes in magma systems documented in plagioclase

1043   zoning patterns: El Misti stratovolcano and Andahua monogenetic cones. Journal of

1044   Volcanology and Geothermal Research 165, 142-162.

1045   https://doi.org/10.1016/j.jvolgeores.2007.06.002.

1046   Shane, P., Naim, I.A., Smith, V.C., Darragh, M., Beggs, K., Cole, J.W., (2008). Silicic recharge of

1047   multiple rhyolite magmas by basaltic intrusion during the 22.6 ka Okareka Eruption Episode,

1048   New Zealand. Lithos 103, 527-549. https://doi.org/10.1016/j.lithos.2007.11.002.

1049   Schnurr, W., Trumbull, R., Clavero, J., Hahne, K., Siebel, W. y Gardeweg, M., (2007). Twenty-five

1050   million years of silicic volcanism in the southern central volcanic zone of the Andes:

1051   Geochemistry and magma genesis of ignimbrites from 25º to 27º S, 67º to 72º W. Journal of

1052   Volcanology   and   Geothermal   Research,   166:   17-46.

1053   https://doi.org/10.1016/j.jvolgeores.2007.06.005.

1054   Scruggs, M. A., Putirka, K. D., (2018). Eruption triggering by partial crystallization of mafic

1055   enclaves at Chaos Crags, Lassen Volcanic Center, California. American Mineralogist 103,

1056   1575-1590. https://doi.org/10.2138/am-2018-6058.

1057   Seggiaro, R., Hongn, F., Folguera, A. and Clavero, J., (2000). Hoja Geológica 2769 – II. Paso de

1058   San Francisco. Boletín 294. Programa Nacional de Cartas Geológicas. 1:250.000.

1059   SEGEMAR.

1060   Shaw, D.M., (2006) Trace elements in magmas. A theoretical treatment. Cambridge University

1061   Press. pp 243. https://doi.org/10.1017/S0016756808004652.

1062   Shcherbakov, V.D., Plechov, P.Y., Izbekov, P.E., Shipman, J.S., (2011). Plagioclase zoning as an

1063   indicator of magma processes at Bezymianny Volcano, Kamchatka. Contribution to

1064   Mineralogy and Petrology 162 (1), 83-99. https://doi.org/10.1007/s00410-010-0584-1.

1065   Shea, T., Hammer, J.E., (2013). Kinetics of cooling- and decompression-induced crystallization in

1066   hydrous mafic-intermediate magma. Journal of Volcanology and Geothermal Research 260,

1067   127-145. https://doi.org/10.1016/j.jvolgeores.2013.04.018.

1068 Siebel, W., Schnurr, W.B.W., Hahne, K., Kraemer, B., Trumbull, R.B., van den Bogaard, P.,

1069   Emmerman, R., (2001). Geochemistry and isotope systematics of small- to medium-volume

1070   Neogene-Quaternary ignimbrites in the southern Central Andes.: evidences for derivation

1071   from andesitic magma source. Chemical Geology 171, 213-237.

1072   https://doi.org/10.1016/S0009-2541(00)00249-7.

1073 Snyder, D., (2000). Thermal effects of the intrusion of basaltic magma into a more silicic magma

1074   chamber and implications for eruption triggering. Earth and Planetary Science Letters 175,

1075   257-273. https://doi.org/10.1016/S0012-821X(99)00301-5.

1076 Sparks, R.S.J., Marshall, L.A., (1986). Thermal and mechanical constraints on mixing between

1077   mafic and silicic magmas. Journal of Volcanology and Geothermal Research 29, 99-124.

1078   https://doi.org/10.1016/0377-0273(86)90041-7.

1079 Stern, C.R., (2004). Active Andean volcanism: its geologic and tectonic setting. Rev. Geol. Chile 31

1080   (2), 161–206. http://dx.doi.org/10.5027/andgeoV31n2-a01.

1081 Streck, M.J., Grunder, A.L., (1999). Enrichment of basalt and mixing of dacite in the rootzone of a

1082   large rhyolite chamber: inclusions and pumices from the Rattlesnake Tuff, Oregon.

1083   Contribution to Mineralogy and Petrology 136, 193-212.

1084   https://doi.org/10.1007/s004100050532.

1085 Streck, M. J., (2008). Mineral textures and zoning as evidence for open system precesses. Rev.

1086   Mineral. Geochem., 69, 595–622.

1087 Suzaño, N., Becchio, R., Sola, A., Fuentes, G., Ortiz, A., (2014). Dominios de basamento del

1088   Paleozoico Inferior en la Sierra de El Peñón, Puna Austral, Provincia de Catamarca. 19th

1089   Congreso Geológico Argentino. Actas, Córdoba, Argentina, pp. 1523–1524.

1090   Tsuchiyama, A., Takahashi, E., (1983). Melting kinetics of a plagioclase feldspar. Contribution to

1091   Mineralogy and Petrology, 84, 345-354. https://doi.org/10.1007/BF01160286.

1092   Turner, J.C. (1961). Estratigrafía del nevado de Cachi y adyacencias. Acta Geológica Lilloana, 3,

1093   191 – 226.

1094   Watson, E.B., Harrison, T.M., 1983. Zircon saturation revisited: temperature and composition

1095   effects in a variety of crustal magma types. Earth and Planetary Science Letters 64 (2), 295-

1096   304.

1097   Whitney, D. L., Evans, B. W., (2010). Abbreviations for names of rock-forming minerals. American

1098   Mineralogist 95: 185-187. https://doi.org/10.2138/am.2010.3371.

1099   Wiebe, R. A., (1996). Mafic-silicic layered intrusions: the role of basaltic injections on magmatic

1100   processes and the evolution of silicic magma chambers. Transactions of the Royal Society

1101   of Edinburgh: Earth Science 87, 233-242. https://doi.org/10.1017/S0263593300006647.

1102

.03

Table 1. Mineral modal compositions of the CPPI rocks

Rock component %	Sample											
	WP	WP	WP	WP	BP	BP	BE	BE	FBE	FBE	CBE	CBE
Glass/vesicles	95	98	92	86	85	90	84	81	67	73	80	85
P.I.	5	2	8	14	15	10	16	19	33	27	20	15
Plagioclase	59	30	45	45	45	40	35	40	42	49	42	39
K-feldspar	27	54	25	32	10	12	tr.	/	/	/	/	/
Quartz	/	5	10	/	/	/	tr.	/	/	/	/	/
Biotie	10	8	15	16	25	27	tr.	/	9	7	27	35
Clinopyroxene	tr.	/	tr.	tr.	2	tr.	30	26	/	/	/	/
Orthopyroxene	tr.	tr.	tr.	/	4	5	18	14	traces	traces	traces	traces
Amphibole	/	/	/	/	10	9	5	2	47	39	23	20
Olivine	tr.	/	/	/	tr.	tr.	5	9	/	/	/	/
Oxides	5	3	5	6	5	7	7	8	2	5	8	6
Apatite	tr.	tr.	tr.	tr.	tr.	tr.	tr.	tr.	tr.	tr.	tr.	tr.
Zircon	tr.	tr.	tr.	tr.	tr.	tr.	/	/	/	/	/	/

tr. = traces amounts; mineral modal porcentajes are calculated excluding the matrix/vesicles %.

.04

Table 2. Whole-rock composition of the CPP products from La-ICP MS analyses

Sample	WP					BP		BE		FBE			CBE	
Oxide	CPP-16-11B	CPP-16-11A	P.B.D.D.	CPP-PB-PRX	P.N.	PB	PBM	PN2	PN1	DD2	DD1	CPP112	DV2	DV1
SiO_2	74.30	73.40	72.70	72.01	72.18	67.40	66.40	55.23	54.60	54.18	56.70	55.60	53.80	53.80
TiO_2	0.25	0.24	0.26	0.23	0.29	0.47	0.48	1.19	1.09	1.50	1.50	1.54	1.40	1.41
Al_2O_3	13.75	13.55	13.57	13.57	14.29	14.49	14.00	15.76	14.25	17.36	16.65	17.10	17.88	17.55
Fe_2O_3	1.64	1.58	1.51	1.46	1.85	3.09	2.95	7.51	7.62	7.73	7.32	7.68	7.56	7.40
FeO	1.48	1.42	1.36	1.31	1.67	2.78	2.65	6.76	6.86	6.96	6.59	6.91	6.80	6.66
MnO	0.05	0.05	0.06	0.06	0.06	0.07	0.07	0.12	0.14	0.13	0.13	0.20	0.13	0.13
MgO	0.38	0.36	0.52	0.35	0.62	1.76	1.47	5.22	6.65	3.97	3.85	3.63	3.31	3.22
CaO	1.41	1.36	1.43	1.22	1.74	2.65	2.56	6.44	6.79	6.90	6.74	6.93	6.00	6.07
Na_2O	3.83	3.74	3.91	3.53	4.04	3.82	3.73	3.38	2.94	3.92	3.75	4.10	3.99	3.87
K_2O	4.81	4.78	4.91	4.87	4.62	4.24	4.13	2.74	2.56	2.70	2.64	2.95	3.15	3.03
P_2O_5	0.08	0.08	0.09	0.08	0.10	n.a	0.17	n.a.	0.29	n.a	0.50	0.49	n.a.	0.66

ppc.	0.63	0.51	1.80	2.54	0.90	1.79	2.74	1.49	1.20	1.21	1.34	1.13	1.47	1.59
Total	100.97	99.49	100.60	100.15	100.52	99.47	98.40	98.33	97.37	98.83	100.39	100.58	97.93	97.99
A/CNK*	0.98	0.98	0.95	1.02	0.96	0.92	0.92	0.78	0.71	0.79	0.78	0.76	0.86	0.85
A/NK**	1.19	1.20	1.16	1.22	1.23	1.33	1.32	1.85	1.87	1.85	1.84	1.72	1.79	1.82

* = cationic ratio $(Na + K + 2Ca)/(Si * Al)$

** = molar $(Al_2O_3/(CaO+Na_2O+K_2O))$

*** = molar $(Al_2O_3/(Na_2O+K_2O))$

ppc. = lost of ignition

.05

Table 3. Microprobe analyses of the CPPI glass

Sample	WP		BP		BE			FBE		CBE	
Oxide	CB-06CPP-5	CB-06CPP-9	PB16-v2	PB16-v5	112a-C9-v1	112b-C1-v1	112a-C9-v4	DD-C1-v1	DD-g2	DV-C4-v2	DV-C4-v11
SiO_2	77.51	77.31	75.51	71.76	72.55	70.87	73.38	69.83	72.64	70.63	68.36
TiO_2	0.03	0.11	0.16	0.16	0.19	0.31	0.14	0.40	0.32	0.45	0.64
Al_2O_3	13.05	12.53	13.20	15.27	15.67	16.10	15.27	15.46	15.51	16.86	16.56
FeO	0.31	0.45	0.95	0.84	0.28	0.37	0.52	0.67	0.43	1.36	1.09
MnO	0.00	0.00	0.05	0.18	0.00	0.00	0.01	0.00	0.00	0.00	0.05
MgO	0.03	0.00	0.07	0.10	0.05	0.04	0.04	0.05	0.04	0.27	0.27
CaO	0.35	0.26	0.81	1.35	1.27	1.17	1.26	1.27	1.23	1.32	1.22
Na_2O	3.02	2.87	3.56	3.82	2.52	2.59	2.78	3.05	4.23	2.61	2.42
K_2O	5.98	6.19	5.66	5.42	5.33	5.36	5.37	5.22	5.06	5.15	5.09
P_2O_5	0.00	0.00	0.04	0.01	0.11	0.03	0.05	0.06	0.07	0.09	0.12
F	0.00	0.00	0.00	0.00	0.00	0.00	0.00	0.00		0.06	0.14
Cl	0.00	0.00	0.15	0.20	0.08	0.08	0.08	0.21	0.17	0.21	0.18
Total	100.28	99.71	100.15	99.10	98.06	96.91	98.91	96.21	99.70	99.01	96.15
A/CNK*	1.08	1.05	0.98	1.05	1.28	1.32	1.20	1.19	1.06	1.37	1.41
A/NK**	1.14	1.10	1.10	1.26	1.58	1.60	1.47	1.45	1.25	1.71	1.74

* = molar $(Al_2O_3/(CaO+Na_2O+K_2O))$

** = molar $(Al_2O_3/(Na_2O+K_2O))$

.06

Table 4. Representative microprobe analyses of CPPI feldspar crystals

Sample	WP plagioclase	BP		BE groundmass	BE phenocry	BE sieve-textured crystals*	FBE phenocrystals**	CBE phenocrystals**	WP K-feldspar	BP	BE

			crystals	sts											
Oxide	112A-C2-Pl2a	112A-C2-Pl2b	PB16-Plp4b	PB16-Plp5b	112a-C1-Plmc1	112a-C3-Pl3c	112b-C5-Pl2c	112a-C1-Pl2b	DD-C1-Pl3c	DD-CNN-Pl2c	106A-C3-Pl1c	106A-C3-Pl1bc	112A-C3-S1c	PB16-b2	PU33-3-1
SiO_2	60.42	54.89	57.60	57.12	56.68	48.16	58.96	57.78	57.11	54.74	54.37	54.77	65.26	66.41	63.87
TiO_2	0.00	0.05	0.00	0.00	0.05	0.07	0.28	0.02	0.17	0.00	0.14	0.12	0.14	0.00	0.12
Al_2O_3	24.40	28.05	26.39	26.36	27.29	33.08	24.58	26.75	26.98	27.96	28.23	28.14	18.46	18.26	19.13
FeO	0.26	0.24	0.26	0.32	0.61	0.52	0.32	0.42	0.32	0.58	0.41	0.37	0.23	0.16	0.21
MnO	0.00	0.00	0.00	0.00	0.00	0.00	0.05	0.00	0.00	0.07	0.12	0.00	0.11	0.00	0.00
MgO	0.05	0.05	0.02	0.00	0.05	0.05	0.00	0.00	0.00	0.06	0.03	0.00	0.01	0.02	0.00
CaO	6.10	10.04	9.04	9.22	9.65	16.18	6.24	8.87	8.71	10.60	11.20	11.01	0.26	0.26	0.31
Na_2O	7.56	5.11	6.14	5.99	5.87	1.97	7.41	6.08	6.01	5.08	4.89	5.06	3.29	3.22	3.12
K_2O	0.96	0.36	0.54	0.45	0.56	0.12	0.81	0.57	0.54	0.33	0.34	0.35	12.35	11.63	11.14
Total	99.8	98.8	100.0	99.5	100.7	100.1	98.6	100.5	99.8	99.4	99.7	99.8	100.1	100.0	97.9
An	29	51	43	45	46	81	30	43	43	53	55	53	1	1	2
Ab	65	47	53	53	51	18	65	54	54	46	43	44	28	29	29
Or	5	2	3	3	3	1	5	3	3	2	2	2	70	69	69

107 An = anorthite; Ab = albite; Or = orthoclase

108 *b = fresh overgrowth; ** c = core; b = rim

Table 5. Microprobe analyses of CPPI clinopyroxene and orthopyroxene grains

Sample	WP opx	BP	BE		BE megacryst	CBE crystal-rich inclusion		BE cpx		WP		BP
Oxide	106A-3b	PB16-A12	112a1-1co	BE-17	112a3-1oc	112a4-2bcu	106A2-2bcu	112a1-3c	112a2-1ccl	112A1-1c	112A6-1	106A2-1c
SiO_2	56.31	53.29	55.22	54.35	55.15	52	54.71	51.96	52.30	53.50	53.59	51.12
TiO_2	0.07	0.35	0.18	0.21	0.30	0.41	0.05	0.33	0.75	0.09	0.21	0.76
Al_2O_3	0.84	2.76	1.41	2.03	2.13	4.55	0.30	3.28	3.44	0.98	0.94	4.44
FeO	13.7	16.53	11.68	11.32	12.49	17.15	16.99	7.05	6.77	9.18	8.91	7.57
MnO	0.60	0.36	0.26	0.24	0.30	0.37	3.95	0.20	0.18	1.12	1.24	0.21
MgO	27.54	25.15	29.28	27.69	29.21	25.01	20.7	16.06	16.34	12.78	12.76	14.95
CaO	0.61	1.06	1.62	1.85	1.34	1.43	1.53	20.38	20.48	21.68	21.40	20.25
Na_2O	0.00	0.11	0.03	0.05	0.03	0.04	0.16	0.38	0.39	0.46	0.48	0.51

Total	99.7	99.6	99.7	97.8	100.9	101.0	98.4	99.6	100.6	99.8	99.5	99.8
$Mg/(Mg+Fe^{2+})$	0.78	0.73	0.82	0.81	0.81	0.72	0.68	0.80	0.81	0.71	0.72	0.78
Wo	1.2	2.2	3.1	3.8	2.6	2.9	3.5	42.26	42.23	46.50	46.41	43.12
En	77.2	71.5	79.1	78.3	78.6	70.1	66.1	46.33	46.88	38.14	38.50	44.30
Fs	21.5	26.4	17.7	18.0	18.8	27.0	30.4	12.88	12.23	18.16	17.76	14.39

Wo = % wollastonite; En = % enstatite; Fs = % ferrosilite Wo = % wollastonite; En = % enstatite; Fs = % ferrosilite.

Table 6. Microprobe analyses of the CPP olivine crystals

Sample	BE				WP	BP
Oxide	112a2l-1c	112a2-2c	112a9-1c	112a1-2	112b8-2	106A4-x
SiO_2	39.16	38.65	39.22	38.28	38.35	41.02
TiO_2	0.00	0.09	0.00	0.16	0.02	0.02
Al_2O_3	0.03	0.01	0.03	0.00	0.03	0.03
FeO	19.87	19.61	23.64	22.42	22.08	18.94
MnO	0.32	0.27	0.21	0.43	0.34	0.55
MgO	40.61	41.21	38.02	39.08	38.23	38.57
Na_2O	0.01	0.00	0.05	0.00	0.02	0.00
K_2O	0.00	0.02	0.01	0.00	0.00	0.07
CaO	0.12	0.12	0.14	0.27	0.11	0.07
P_2O_5	0.06	0.04	0.04	0.05	0.00	0.08
F	0.00	0.00	0.00	0.02	0.16	0.00
Cl	0.03	0.01	0.01	0.00	0.00	0.02
Total	100.20	100.02	101.39	102.51	99.35	99.31
Cation (apfu)						
Si	1.01	0.99	1.13	0.99	1.01	1.07
Ti	0.00	0.00	0.00	0.00	0.00	0.00
Al	0.00	0.00	0.00	0.00	0.00	0.00
Cr	0.00	0.00	0.00	0.00	0.00	0.00
Fe3	0.00	0.01	0.00	0.01	0.00	0.00
Fe2	0.43	0.41	0.57	0.47	0.48	0.41
Mn	0.01	0.01	0.01	0.01	0.01	0.01
Mg	1.56	1.58	1.29	1.51	1.50	1.50
Ca	0.00	0.00	0.00	0.01	0.00	0.00
Mg#	0.78	0.79	0.69	0.76	0.76	0.78
Te	0.35	0.29	0.28	0.47	0.38	0.63

Fo	78.06	78.57	69.01	75.02	75.12	77.83
Fa	21.43	20.97	30.48	24.14	24.34	21.44
Ca-Ol	0.16	0.16	0.23	0.37	0.16	0.10

Te = tephroite Fo = forsterite; Fa = fayalite; Ca-Ol = calcic olivine

110

Table 7. Represestative compositions of CPPI amphibole and biotite crystals, and amphibole thermo-baro-hygrometric results from Ridolfi and Renzulli, (2012) method

Sample	FBE amp		FBE c		CBE core		CBE rim		BP core	BP rim
Oxide	DD-1b	DD-3b	DD-1b	DD1-c	DV2-F11c	DV-11c	DV-A2b	DV-C6b	PB16-A11c	PB16-A10b
SiO_2	42.24	41.8	39.03	40.18	40.23	41.02	41.60	42.56	41.60	42.15
TiO_2	3.19	3.25	4.98	3.54	4.73	3.7	4.15	3.48	4.31	4.42
Al_2O_3	11.01	10.94	13.66	12.9	12.47	12.37	12.61	11.89	12.18	11.72
FeO	14.09	14.63	15.21	13.1	12.42	12.3	13.09	13.03	11.75	11.70
MnO	0.28	0.41	0.28	0.27	0.18	0.38	0.25	0.42	0.07	0.10
MgO	12.46	12.33	10.67	12.39	12.75	13.59	12.60	12.98	12.77	13.27
CaO	11.35	11.65	11.94	11.49	11.71	11.48	11.65	11.75	11.76	11.94
Na_2O	2.11	2.36	2.51	2.5	2.70	2.44	2.62	2.52	2.26	2.26
K2O	1.23	1.25	1.01	1.03	0.94	0.96	1.06	0.99	0.98	1.12
F	0.16	0.30	0.00	0.22	0.00	0.03	0.08	0.00	0.00	0.32
Cl	0.12	0.10	0.06	0.02	0.05	0.05	0.02	0.06	0.04	0.07
H_2O_{calc}	1.80	1.80	1.80	1.80	1.80	1.80	1.80	1.80	1.80	1.80
Anhydrous Total	98.25	99.01	99.35	97.64	98.19	98.31	99.74	99.68	97.71	99.07
$Mg/(Mg+Fe^{2}+)$	0.67	0.66	0.63	0.69	0.72	0.72	0.68	0.68	0.71	0.72
Fe/(Fe+Mg)	0.33	0.34	0.37	0.32	0.28	0.28	0.32	0.32	0.29	0.28
T Rid12[a] (°C)	940	953	1033	1003	1013	994	991	967	984	979
P Rid12[b] (Kbar)	923	955	1007	994	1035	1034	1012	1004	968	991
H_2O[c] Rid12 (wt %)	4.73	4.22	4.66	4.87	4.84	5.13	5.62	5.78	4.31	5.24

111

112

113

Table 7 continuation

Sample	BE microcx	BE corona	BE phenocx	WP biotite	BP	BE	FBE	CBE	
Oxide	112a7-3mc	112a1-co	CPP112b-2	112A2-1	CB-2-c2-5	112a4-2c	DD1-1c	DV1-2ot	DV1.Bt2crx*
SiO2	40.34	43.04	41.47	36.12	36.83	36.06	36.11	36.58	35.81
TiO2	4.74	2.34	2.70	5.48	4.78	5.50	5.71	5.87	5.43
Al2O3	13.03	11.2	12.99	13.16	13.42	14.32	14.25	14.73	14.86
FeO	12.95	12.63	11.27	17.94	16.94	17.02	15.29	14.03	14.19
MnO	0.18	0.24	0.17	0.47	0.13	0.26	0.29	0.11	0.17
MgO	13.12	14.32	14.09	12.71	13.32	13.64	14.36	15.19	15.10
CaO	11.45	11.05	11.79	0.00	0.03	0.00	0.01	0.00	0.01
Na2O	2.14	2.16	2.45	0.50	0.74	0.61	0.74	1.03	1.09
K2O	0.96	0.91	1.07	9.39	10.74	8.68	8.66	8.29	8.40
F	0.16	0.16	0.12	0.43	0.00	0.21	0.29	0.00	0.21
Cl	0.05	0.05	0.05	0.13	0.00	0.07	0.10	0.07	0.06
H2Ocalc	1.80	1.80	1.80	3.72	3.96	3.88	3.84	4.02	3.87
Anhydrous Total	99.12	98.10	98.17	96.33	96.92	96.38	95.82	95.90	95.33
Mg/(Mg+Fe2+)	0.70	0.73	0.76	0.56	0.58	0.59	0.62	0.66	0.65
Fe/(Fe+Mg)	0.30	0.27	0.24	0.44	0.42	0.41	0.38	0.34	0.35
T Rid12a (°C)	/	/	1000						
P Rid12b (Kbar)	/	/	988						
H2Oc Rid12 (wt %)	/	/	7.94						

114   a = calculated amphibole temperatures from the Ridolfi and Renzulli,(2012) thermometer

115   b = calculated amphibole pressures from the Ridolfi and Renzulli,(2012) barometer

116   c = calculated H2Oliq from the Ridolfi and Renzulli,(2012) hygrometer

117

118

119

Highlights

- Pleistocene rhyolitic ignimbrite with multi-banded pumice clasts (mafic enclaves)

- Chemical hybridization of rhyolite and basalt to form dacitic rocks

- Enclave amphibole zoning reflecting re-equilibration in the rhyolitic reservoir

- Pre-eruptive cooling stage of rhyolitic melt to 800 °C at a depth of 2.6 Kbar

Bardelli, Lorenzo Facultad de Ciencias Naturales, Universidad de Salta, Instituto Geonorte, CONICET; lorenzobardelli4@gmail.com

Arnosio, Marcelo, Facultad de Ciencias Naturales, Universidad de Salta, Instituto Geonorte, CONICET chinoarnosio@yahoo.com.ar

Báez, Walter, Facultad de Ciencias Naturales, Universidad de Salta, IBIGEO, CONICET; focobaez@hotmail.com

Suzaño, Nestor, Universidad Nacional de Jujuy, IBIGEO, CONICET; nestormusic10@gmail.com

Becchio, Raúl, Facultad de Ciencias Naturales, Universidad de Salta, CONICET; tatobecchio@yahoo.com

Viramonte, José, Facultad de Ciencias Naturales, Universidad de Salta, IBIGEO, CONICET; joseviramonte@yahoo.com.ar

Bustos, Emilce, Facultad de Ciencias Naturales, Universidad de Salta, IBIGEO, CONICET, emilcebustos@gmail.com

Bertea Esteban Santiago, Facultad de Ciencias Naturales, Universidad de Salta, IBIGEO, CONICET; estebansantiagobertea@gmail.com

Declaration of interest "none"